International Journal of Mechanical Sciences 312 (2026) 111280

Contents lists available at ScienceDirect

International Journal of Mechanical Sciences

journal homepage: www.elsevier.com/locate/ijmecsci

Model-free sequential design of absorbers for customized vibration control

Hangxing LI, Waion WONG *, Li CHENG *

Department of Mechanical Engineering, The Hong Kong Polytechnic University, Hong Kong SAR, China

ARTICLE INFO

Keywords:
Distributed absorbers design
Complex structure
Complex coupling
Model-free design approach
Customized vibration control
Sequential design strategy

ABSTRACT

Optimal design of distributed vibration absorbers for controlling broadband vibration of structures is challenging, mainly because of the modal coupling incurred inside the structure as well as the interplay among multiple absorbers. Without analytical solutions, absorber design usually resorts to numerical optimizations over the full parameter space, which is computationally intensive alongside the risk of being trapped into local optima. Meanwhile, most existing methods are model based, mostly numerical ones, thus adding additional difficulties when the structure is complex with uncertain parameters which are difficult to be accurately apprehended. In this paper, based on the structural response (either simulated or experimentally measured), we propose a model-free and sequential approach for the design of distributed absorbers over an arbitrarily given thin-walled structure to achieve pre-defined target vibration reduction. The proposed approach involves a systematic three-step procedure. Upon identifying the Excitation-Dependent Representative Basis (EDRB) of the primary structure, locations of the absorbers are first determined to ensure their strong coupling with the targeted and higher-frequency EDRB while minimizing the interaction with the lower-frequency ones. Subsequently, absorber masses are determined through an inverse design approach, followed by the optimization of their uncoupled frequencies and damping coefficients through an iteration procedure in which only two parameters are involved. The effectiveness of the proposed approach is validated through both numerical simulations on representative cases and experiments on a complex structure.

1. Introduction

Controlling structural vibration and its sound radiation is of significant practical relevance for numerous engineering applications [1–3]. While high-frequency vibrations can be effectively mitigated using energy dissipation materials, dynamic absorbers remain one of the most effective means to deal with low-frequency problems [4–6].

Studies on dynamic absorbers have been extensive and long-lasting, as reviewed by many papers [7–20]. A single absorber is effective only over a narrow frequency range dominated by a single vibrational mode [21]. To achieve broadband vibration control, multiple absorbers should be deployed [22–24], with their respective positions and physical parameters properly designed such as mass, frequency and damping. The large number of interdependent parameters makes the design process extremely challenging. When the vibration modes of the structures are well separated, modal interaction can be simplified or even neglected to some extent, thus simplifying the design process. As such, optimal absorber parameters can be derived using traditional fixed-point theory [25–28]. In the case of closely spaced resonant frequencies (of the primary structure or of the multiple absorbers targeting the same structural mode), the coupling between different modes with the add-on absorbers or the strong coupling among the absorbers themselves need be carefully apprehended [29,30]. The challenge arising from this lies in incorporating the complex coupling into the design process without a substantial increase in optimization complexity.

Owing to their ability in learning complex coupling features directly from data, machine learning techniques hold significant promise to streamline absorber design in complex systems [31,32], a topic deserving deep and systematic investigation. Another method consists in attaching absorbers at tactic positions to simplify their complex interactions with the primary structure. This makes it possible to obtain optimal absorber parameters through the analysis of a coupled system of a single absorber and a single mode [33]. To achieve this, it is essential to ensure the weak coupling between absorbers and untargeted structural modes. However, locations chosen this way may not be optimal. Consequently, this strategy might affect the vibration suppression performance on one hand, and may even not be achievable with multiple absorbers on the other hand. To alleviate the problem, the complex

* Corresponding authors.
E-mail addresses: wai.on.wong@connect.polyu.hk (W. WONG), li.cheng@polyu.edu.hk (L. CHENG).

https://doi.org/10.1016/j.ijmecsci.2026.111280
Received 20 November 2025; Received in revised form 14 January 2026; Accepted 16 January 2026
Available online 17 January 2026

coupling between multiple absorbers and structural modes need to be considered when optimizing absorber parameters. As there is usually no analytical solution available for the coupled system, numerical optimizations are commonly adopted to search for the optimal parameters within the full parameter space [34–37]. This obviously relies on accurate structural models and the accurate identification of excitations, both of which turn out to be difficult to be accurately acquired in practice [38,39]. In addition, the above methods are inherently time-consuming for large structures and the solution can easily be trapped to local optima. Therefore, the strong reliance of the design and optimization methods on simulation models and the complex interplay among numerous design parameters are seen as two major bottlenecks in the design of multiple dynamic absorbers for effective and broadband vibration reduction. This motivates the present study, in which an effective solution is proposed to solve the aforementioned issues. More specifically, a model-free and sequential design procedure is proposed for designing distributed absorbers for an arbitrarily given thin-walled structure to achieve pre-defined and targeted vibration reduction.

The salient features of the approach are its model-free nature and the sequential determination of the major absorber parameters in the context of multiple absorbers design. In the proposed approach, *in-situ* structural dynamics, which can either be experimentally measured or numerically simulated, serves as the basis of the design. Through principal component analysis, each identified Excitation Dependent Representative Basis (EDRB) can be used to characterize the structural response caused by either a single or multiple closely-spaced structural modes [40,41], thus circumventing the coupling complication arising from the overlapping of structural modes [29]. Note the idea of using EDRB has been partially exploited by other existing works. For example, Wu and Li optimized absorber parameters by exclusively considering the interaction between one EDRB and one vibration absorber [41]. In the case of multiple absorbers for suppressing multiple resonance peaks, however, the mutual coupling among absorbers on top of their interaction with the EDRBs of the primary structure add tremendous difficulties in the design, an issue which has not been well addressed in the literature. Besides, traditional absorber design methodologies typically rely on predefined mass ratios, making the attainment of desired and pre-defined vibration suppression more difficult if not impossible. The method proposed in this paper provides a general solution to address the above issues. Derived from the response of the structural EDRB, the optimal location of the absorbers and their physical parameters can be sequentially designed to achieve customized vibration control. In a broader sense, the formulation presented in this paper is also useful in understanding the complex interaction between a primary structure and multiple add-on dynamic absorbers. In summary, this paper attempts to make three key contributions:

1) a location selection strategy that accounts for mutual modal coupling, enabling the determination of the optimal absorber placement using only experimentally measured data;
2) a sequential design method that simplifies complex coupling to streamline the absorber design process while preserving essential resonant interactions in the structure; and
3) an inverse design method for achieving customized vibration response.

The outline of the paper is as follows. Section 2 lays down the theoretical foundation and establishes the proposed methodology. Section 3 substantiates the proposed approach and demonstrates its efficacy in dealing with three typical cases. Using a plate as an illustrative example, the first case evaluates the feasibility of the proposed inverse design method in meeting stringent response control requirements and demonstrates the superior performance of the proposed sequential design method. The second case examines the applicability of the design method to structures with symmetric modes, highlighting its effectiveness in achieving all-equal-peak response control. The last case applies the method to a rocket fairing structure, demonstrating its suitability for dealing with complex structures subjected to distributed loads. Section 4 experimentally validates the proposed approach using a complex structure, and the main conclusions are summarized in Section 5.

2. Theoretical formulation and design methodology

Consider a general structure coupled with multiple dynamic absorbers shown in Fig. 1. The structure is loaded by an excitation force $\mathbf{F}(t)$, with its transverse response represented by $\mathbf{X}(t)$. A cluster of absorbers is attached to the structure, in which the mass, stiffness, damping coefficient, position, and response of the nth absorber are denoted by m_n, k_n, c_n, $\mathbf{r}_n$ and x_n, respectively. We next employ this model to develop the proposed model-free sequential design method. It should be noted that the present model is used solely for illustrative purposes, no model information is employed in the subsequent derivations.

Motion equation of this coupled system can be cast into the following form:

$$\begin{aligned}\mathbf{M}\ddot{\mathbf{X}}(t)+\mathbf{K}\mathbf{X}(t)=\mathbf{F}(t)+\sum_{n=1}^{N}\left[k_n\left(x_n(t)-\mathbf{b}_n^T\mathbf{X}(t)\right)+c_n\left(\dot{x}_n(t)-\mathbf{b}_n^T\dot{\mathbf{X}}(t)\right)\right]\mathbf{b}_n\\ k_n\left(x_n(t)-\mathbf{b}_n^T\mathbf{X}(t)\right)+c_n\left(\dot{x}_n(t)-\mathbf{b}_n^T\dot{\mathbf{X}}(t)\right)=-m_n\ddot{x}_n(t)\end{aligned}, \tag{1}$$

where $\mathbf{M}$ and $\mathbf{K}$ are the mass and stiffness matrices of the primary structure; N the number of absorbers; $\mathbf{b}_n$ a column vector representing the position of the nth absorber, with non-zero element (equal to 1) only at the degree of freedom corresponding to the connection point between the absorber and the primary structure.

With a zero-initial condition, the Laplace transform of the above equation writes

$$\begin{aligned}s^2\mathbf{M}\mathbf{X}(s)+\mathbf{K}\mathbf{X}(s)=\mathbf{F}(s)+\sum_{n=1}^{N}\left[k_n\left(x_n(s)-\mathbf{b}_n^T\mathbf{X}(s)\right)+sc_n\left(x_n(s)-\mathbf{b}_n^T\mathbf{X}(s)\right)\right]\mathbf{b}_n\\ k_n\left(x_n(s)-\mathbf{b}_n^T\mathbf{X}(s)\right)+sc_n\left(x_n(s)-\mathbf{b}_n^T\mathbf{X}(s)\right)=-s^2m_nx_n(s)\end{aligned}, \tag{2}$$

where s represents the complex number.

This matrix equation, in principle, can be decomposed in modal space, which, however, is difficult to be accurately determined through mathematical modelling for complex structures. To solve this problem, we project this equation into the vector space spanned by the so-called Excitation-Dependent Representative Basis (EDRB) [40,41]. The use of EDRB has two advantages: a) EDRB can be obtained by conducting Principal Component Analysis (PCA) or Singular Value Decomposition (SVD) on structural response that can be measured experimentally (as shown in Fig. 1 where a laser-vibrometer is deployed), which is free of the simulation model; b) structural response superimposed by multiple dense modes can be represented by one EDRB, thus reducing the dimension of the matrix equation, which is pivotal for the design of absorbers to achieve broadband response control. Therefore, the acquired structural response can be decomposed as

$$\mathbf{X}(s)=\mathbf{U}\Sigma\mathbf{V}^H(s), \tag{3}$$

where the columns of matrix $\mathbf{U}$ and $\mathbf{V}(s)$ represent eigenvectors of response in space and frequency domains, respectively. Singular value matrix $\mathbf{\Sigma}$ is a rectangular diagonal matrix with non-negative real numbers on the diagonal. The number of retained singular vectors is determined using a cumulative energy criterion: the smallest subset of the dominant singular vectors is retained such that the sum of their corresponding singular values accounts for at least 90% of the total sum of all singular values.

Substituting Eq. (3) into Eq. (2) yields

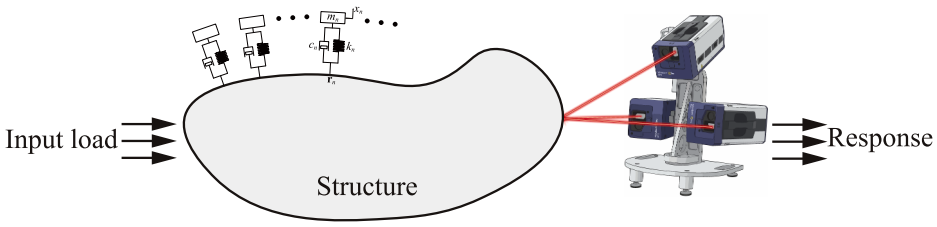

Fig. 1. Schematic of a generic structure coupled with multiple absorbers. Only the measured response $\mathbf{X}(t)$ is utilized in the absorber design process.

$$\left(s^2\mathbf{M}^{\mathrm{U}}+\mathbf{K}^{\mathrm{U}}+\sum_{n=1}^{N}h_n(s)\boldsymbol{\theta}_n\boldsymbol{\theta}_n^T\right)\boldsymbol{\Sigma}\mathbf{V}^H(s)=\mathbf{F}^{\mathrm{U}}(s), \tag{4}$$

where

$$\begin{cases}\mathbf{M}^{\mathrm{U}}=\mathbf{U}^T\mathbf{M}\mathbf{U},\ \mathbf{K}^{\mathrm{U}}=\mathbf{U}^T\mathbf{K}\mathbf{U},\ \mathbf{F}^{\mathrm{U}}(s)=\mathbf{U}^T\mathbf{F}(s),\ \boldsymbol{\theta}_n=\mathbf{U}^T\mathbf{b}_n\\ h_n=\dfrac{s^2m_n\left(2\xi_n s\omega_n+\omega_n^2\right)}{s^2+2\xi_n s\omega_n+\omega_n^2},\ \xi_n=\dfrac{c_n}{2m_n\omega_n},\ \omega_n=\sqrt{\dfrac{k_n}{m_n}}\end{cases}. \tag{5}$$

Note that although Eq. (4) is derived based on classical dynamic M-K-C vibration absorbers, the above established formalism is also applicable to other types of absorbers [42–47] (See Appendix B for more details), such as the active absorber [48–51], inerter-based dynamic vibration absorbers [52–61], electromagnetic shunt dampers [62–72], piezoelectric shunt dampers [73–86] and Helmholtz resonators [87–98] in the case of cavity noise control, etc. The corresponding governing equation for each case can be readily obtained by substituting the corresponding transfer function h_n and coupling coefficient vector $\boldsymbol{\theta}_n$.

As previously mentioned, the structural response superimposed by multiple dense modes can be represented by a single EDRB, so that the peaks of the obtained EDRB curves can be regarded as well separated. Indeed, if two EDRBs were too close in frequency, they would have been consolidated into a single EDRB during the construction process. This built-in filtering mechanism ensures that the final set of EDRBs always satisfies the required separation for approximation. Therefore, coupling between different EDRBs can be ignored and the response of a single EDRB can be written as

$$V_i(s)=\frac{F_i^{\mathrm{U}}(s)/\sigma_i}{s^2M_i^{\mathrm{U}}+K_i^{\mathrm{U}}+\sum_{n=1}^{N}\frac{s^2m_n\left(2\xi_n s\omega_n+\omega_n^2\right)}{s^2+2\xi_n s\omega_n+\omega_n^2}\vartheta_{i,n}^2}, \tag{6}$$

where M_i^{U}, K_i^{U}, F_i^{U}, $\vartheta_{i,n}$ and σ_i are the ith element of $\mathbf{M}^{\mathrm{U}}$, $\mathbf{K}^{\mathrm{U}}$, $\mathbf{F}^{\mathrm{U}}$, $\boldsymbol{\theta}_n$ and $\boldsymbol{\Sigma}$, respectively. In this paper, $V_i(s)$ and $F_i^{\mathrm{U}}(s)$ are referred to as the generalized coordinate and generalized force of the ith EDRB, respectively.

It should be noted that the decoupling approximation between EDRBs is not an ad hoc simplification but a natural consequence of the EDRB formulation itself, which was originally introduced to address the very challenge of strong modal coupling in broadband vibration control.

2.1. Position selection of absorbers

In Eq. (6), the ith absorber targets the resonance response of the ith EDRB. Since multiple absorbers are attached on the primary structure, the presence of other absorbers ($n \neq i$) complicates the design. We can therefore rewrite this equation to obtain an equivalent single absorber model as

$$V_i(s)=\frac{F_i^{\mathrm{U}}(s)}{\vartheta_{i,i}^2\sigma_i}\frac{1}{s^2\mathbb{M}_i+\mathbb{K}_i+\frac{s^2m_i\left(2\xi_i s\omega_i+\omega_i^2\right)}{s^2+2\xi_i s\omega_i+\omega_i^2}}, \tag{7}$$

where

$$\mathbb{M}_i=\frac{M_i^{\mathrm{U}}+\sum_{n=1,n\neq i}^{N}\frac{m_n\left(2\xi_n s\omega_n+\omega_n^2\right)}{s^2+2\xi_n s\omega_n+\omega_n^2}\vartheta_{i,n}^2}{\vartheta_{i,i}^2},\ \mathbb{K}_i=\frac{K_i^{\mathrm{U}}}{\vartheta_{i,i}^2}. \tag{8}$$

Eq. (7) holds the same form as the traditional 2-DoF absorber model [28]. Optimal frequency, damping coefficient and maximum vibration amplitude can therefore be obtained according to the fixed-point theory as

$$\gamma_i=\frac{\omega_i}{\Omega_i}=\frac{1}{1+\mu_i},\ \xi_i=\sqrt{\frac{3\mu_i}{8(1+\mu_i)}},\ V_i(s)|_{\max}=\frac{F_i^{\mathrm{U}}(s)}{\vartheta_{i,i}^2\mathbb{K}_i\sigma_i}\sqrt{\frac{2+\mu_i}{\mu_i}}, \tag{9}$$

where

$$\Omega_i=\sqrt{\frac{\mathbb{K}_i}{\mathbb{M}_i}},\ \mu_i=\frac{m_i}{\mathbb{M}_i}. \tag{10}$$

For better performance, the maximum amplitude $V_i(s)|_{\max}$ needs to be minimized. As shown in Eq. (9), $V_i(s)|_{\max}$ contains two variables $\vartheta_{i,i}$ and $\vartheta_{i,n}$ which are functions of locations of the ith and the nth absorbers. This can be leveraged to guide the selection of absorber locations as follows:

a) $V_i(s)|_{\max}$ is inversely proportional to $\vartheta_{i,i}^2$, indicating that the ith absorber needs to be placed at the position to make the amplitude of $\vartheta_{i,i}$ large enough.
b) $V_i(s)|_{\max}$ has a positive correlation with $\mathbb{M}_i$, which means the positions of the remaining absorbers need to be chosen to make $\mathbb{M}_i$ small enough. The effective mass of the absorber $\frac{m_n\left(2\xi_n s\omega_n+\omega_n^2\right)}{s^2+2\xi_n s\omega_n+\omega_n^2}$ is a positive value before its resonance frequency, and a negative value after, as shown in Fig. 2. Around resonance frequency Ω_i of the ith EDRB, the effective mass of absorber is a positive value if $\omega_n > \Omega_i$, which will increase value of $\mathbb{M}_i$. The absorber therefore needs to be placed in

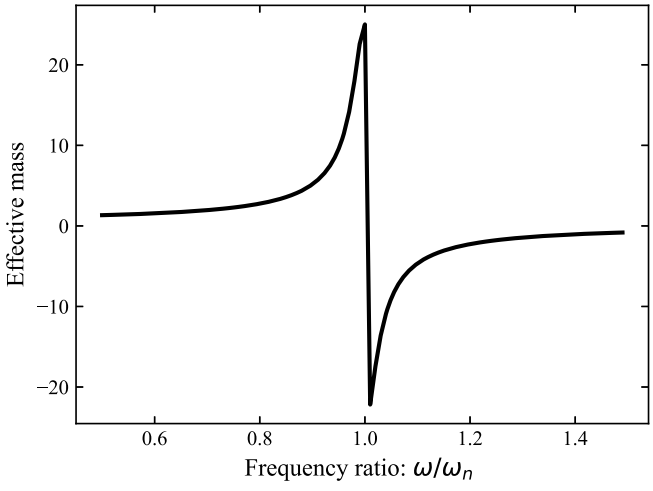

Fig. 2. Effective mass $\frac{m_n\left(2\xi_n s\omega_n+\omega_n^2\right)}{s^2+2\xi_n s\omega_n+\omega_n^2}$ of absorber. The effective mass is a positive value before its resonance frequency, and a negative value after.

such a way that the amplitude of $\vartheta_{i,n}$ is small enough. Conversely, absorber with $\omega_n < \Omega_i$ should be placed to make $\vartheta_{i,n}$ large enough.

Summarizing these two observations, we can get the ith row of Table 1, which leads the principle for the position selection of absorbers. In this table, elements at the diagonal and the lower triangle (shadowed area) should be made as large as possible and those within the upper triangle of table should be made as small as possible.

The optimal location of the ith absorber can then be determined by the ith column Table 1. Information/position choice given by the entire column are generally redundant, so we can prioritize these elements and select the first few to use. As mentioned, $V_i(s)|_{\max}$ has a direct inverse proportional relationship with $\vartheta_{i,i}^2$, the diagonal elements in this table are therefore the most important entries. The adjacent elements with closer resonance frequencies play a secondary role in controlling structural response. Therefore, diagonal conditions need to be used first to determine the optimal absorber locations. Only if the locations cannot be met by the diagonal elements, adjacent conditions can be used. The flowchart for the location selection strategy according to Table 1 is shown in the flowchart in Fig. 3.

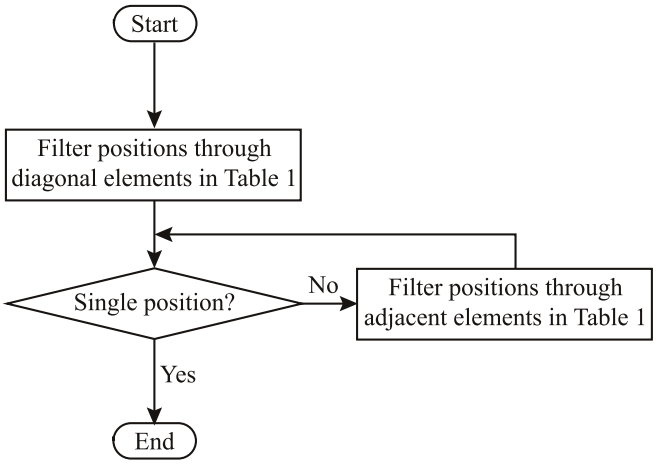

Fig. 3. Flowchart for selecting absorber positions. Diagonal conditions are to be applied first, followed by adjacent conditions.

2.2. Customization of vibration control

Eq. (9) shows the dominant role of the absorber mass on the maximum response of the primary structure. Therefore, to achieve the desired and pre-defined vibration reduction target, we need to determine the corresponding mass distribution of absorbers. This is an inverse design problem to be discussed in this section.

The average Power Spectral Density (PSD) of the structure can be expressed as

$$S_{\mathbf{xx}}(s) = \frac{\mathbf{X}^H(s)\mathbf{X}(s)}{N_{dim}}, \tag{11}$$

where N_{dim} is the number of the measurement/estimation points.

Substitution of Eq. (3) into Eq. (11) gives

$$S_{\mathbf{xx}}(s) = \frac{\mathbf{V}(s)\mathbf{\Sigma}^H\mathbf{M}^{\mathrm{U}}\mathbf{\Sigma}\mathbf{V}^H(s)}{m}, \tag{12}$$

where

$$\mathbf{M}^{\mathrm{U}} = \Delta S m_s \mathbf{U}^H\mathbf{U},\ \ m = \Delta S m_s N_{dim}, \tag{13}$$

in which m_s is the normalized mass [29]; ΔS denotes the surface area of the sampling unit, as shown in Fig. 4 and m represents the total mass of the primary structure.

Focusing on the resonance response of the ith EDRB, Eq. (12) can be expressed as

$$S_i(s) = \frac{\sigma_i^2 M_i^{\mathrm{U}} V_i^2(s)}{m}. \tag{14}$$

As shown in Fig. 2, the effective mass of an absorber can be considered a constant value at the frequency away from its resonance frequency. According to Eq. (9), when the mass ratio of the absorber is much smaller than 1 (which is generally the case for resonant absorbers), the frequency ratio of the absorber is very close to 1 and the damping coefficient is usually small. Taking these two assumptions, i.e. $\gamma_n = 1,\ \xi_n = 0$, the constant value at $s = \mathrm{j}\Omega_i$ of Eq. (8) can be

Table 1
Principle for the position selection of absorbers.

	DVA_1	DVA_2	⋯	DVA_I
EDRB_1	$\lvert\vartheta_{1,1}\rvert$	$\lvert\vartheta_{1,2}\rvert$	⋯	$\lvert\vartheta_{1,I}\rvert$
EDRB_2	$\lvert\vartheta_{2,1}\rvert$	$\lvert\vartheta_{2,2}\rvert$	⋯	$\lvert\vartheta_{2,I}\rvert$
⋮	⋮	⋮	⋱	⋮
EDRB_I	$\lvert\vartheta_{I,1}\rvert$	$\lvert\vartheta_{I,2}\rvert$	⋯	$\lvert\vartheta_{I,I}\rvert$

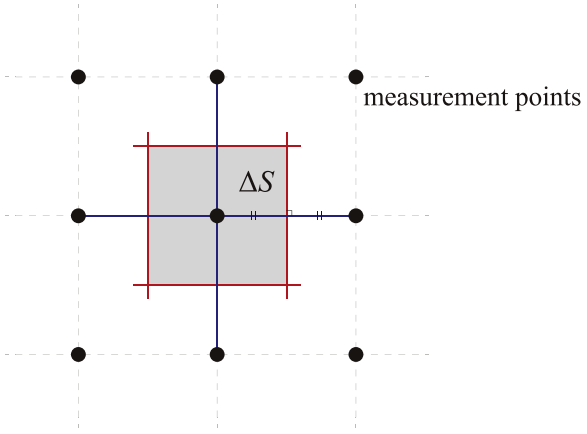

Fig. 4. Surface area of a sampling unit.

approximated as

$$\mathbb{M}_i = \frac{M_i^{\mathrm{U}} + \sum_{n=1,n\neq i}^{N} \frac{m_n\Omega_n^2}{-\Omega_i^2+\Omega_n^2}\vartheta_{i,n}^2}{\vartheta_{i,i}^2},\ \ \mathbb{K}_i = \frac{K_i^{\mathrm{U}}}{\vartheta_{i,i}^2}. \tag{15}$$

Substituting Eqs. (9) and (15) into Eq. (14) yields

$$S_i(s)|_{\max} = \frac{M_i^{\mathrm{U}}\left[F_i^{\mathrm{U}}(s)\right]^2}{m\vartheta_{i,i}^6\mathbb{K}_i^2}\frac{2\left(M_i^{\mathrm{U}} + \sum_{n=1,n\neq i}^{N}\frac{m_n\Omega_n^2}{-\Omega_i^2+\Omega_n^2}\vartheta_{i,n}^2\right) + \vartheta_{i,i}^2 m_i}{m_i}, \tag{16}$$

where m_i and m_n are the variables to be designed. So far only $F_i^{\mathrm{U}}(s)$ is unknown. According to Eq. (6), before attaching absorbers, one has

$$V_i(s) = F_i^{\mathrm{U}}(s)H_i^{\mathrm{U}}(s) = \frac{F_i^{\mathrm{U}}(s)}{\sigma_i}\frac{1}{s^2M_i^{\mathrm{U}} + K_i^{\mathrm{U}}}, \tag{17}$$

where $V_i(s)$ is the ith column of matrix $\mathbf{V}(s)$ in Eq. (3) and σ_i the ith diagonal element of singular value matrix $\mathbf{\Sigma}$ in Eq. (3). M_i^{U} can be obtained by Eq. (13), $K_i^{\mathrm{U}} = \left(\Omega_i^{\mathrm{U}}\right)^2 M_i^{\mathrm{U}}$, where Ω_i^{U} can be determined by finding the peak frequency of $V_i(s)$. $F_i^{\mathrm{U}}(s)$ is the only unknown parameter in Eq. (17) which can therefore be obtained by the following optimization:

$$\underset{F_i^{\mathrm{U}}(s)}{\operatorname{argmin}}\left\|V_i(s)-\frac{F_i^{\mathrm{U}}(s)}{\sigma_i}\frac{1}{\left[s^2+\left(\Omega_i^{\mathrm{U}}\right)^2\right]M_i^{\mathrm{U}}}\right\|_2 \omega \in \left(0.8\Omega_i^{\mathrm{U}},\ 0.95\Omega_i^{\mathrm{U}}\right)\cap\left(1.05\Omega_i^{\mathrm{U}},\ 1.2\Omega_i^{\mathrm{U}}\right). \tag{18}$$

Since absorbers are effective only over a narrow frequency band around the resonant frequency of the primary structure, the analysis based on Eq. (18) can be restricted to a small neighbourhood around the EDRB resonant frequency Ω_i^{U}. Within this narrow band, the generalized force $F_i^{\mathrm{U}}(s)$ may be reasonably approximated as constant. Furthermore, a direct analytical evaluation of Eq. (18) at the exact resonant frequency yields an unbounded response, which is non-physical and inconsistent with real-world measurements that inherently include damping and other limiting effects. Therefore, in the design process, frequencies infinitesimally close to Ω_i^{U} are deliberately excluded to avoid singularity and ensure a practical solution.

Assuming that the absorber design aims to satisfy the condition $S_i|_{\max} = T_i$, according to Eqs. (16) and (18), the following equation can be obtained.

$$\left(\frac{m\vartheta_{i,i}^6\mathbb{K}_i^2T_i}{2M_i^{\mathrm{U}}\left[F_i^{\mathrm{U}}(s)\right]^2}-\frac{\vartheta_{i,i}^2}{2}\right)m_i-\sum_{n=1,n\neq i}^{N}\frac{\Omega_n^2\vartheta_{i,n}^2}{-\Omega_i^2+\Omega_n^2}m_n=M_i^{\mathrm{U}}. \tag{19}$$

For I absorbers, I equations can be obtained, expressed as

$$\begin{bmatrix} \frac{m\vartheta_{1,1}^6\mathbb{K}_1^2T_1}{2M_1^{\mathrm{U}}\left[F_1^{\mathrm{U}}(s)\right]^2}-\frac{\vartheta_{1,1}^2}{2} & \cdots & -\frac{\Omega_N^2\vartheta_{1,N}^2}{-\Omega_1^2+\Omega_N^2} \\ \vdots & \ddots & \vdots \\ -\frac{\Omega_1^2\vartheta_{I,1}^2}{-\Omega_I^2+\Omega_1^2} & \cdots & \frac{m\vartheta_{I,I}^6\mathbb{K}_I^2T_I}{2M_I^{\mathrm{U}}\left[F_I^{\mathrm{U}}(s)\right]^2}-\frac{\vartheta_{I,I}^2}{2} \end{bmatrix}\begin{bmatrix} m_1 \\ \vdots \\ m_I \end{bmatrix}=\begin{bmatrix} M_1^{\mathrm{U}} \\ \vdots \\ M_I^{\mathrm{U}} \end{bmatrix}. \tag{20}$$

Solving this matrix equation, the mass distribution of all absorbers can be determined to achieve the prescribed vibration reduction level.

2.3. Sequential design of absorber parameters

By now, the optimal positions and the mass distribution of absorbers have been determined. We proceed to design the uncoupled resonance frequencies of the absorbers (before they are installed on the primary structure) and their damping coefficients.

As shown in Eq. (2), the damping force $f_c = sc_n\left(x_n(s)-\mathbf{b}_n^T\mathbf{X}(s)\right)$ of an absorber is positively proportional to frequency. For high frequency response, damping can provide significant coupled force. For low frequency response, however, the coupled force of absorber is mainly controlled by the inertia force and stiffness force. As shown in Eq. (5), only when $\omega < \omega_n$, $2\xi_n\omega \ll \omega_n$, the damping force (imaginary part) in h_n can be removed, which inspires a sequential design method. When designing the 1st absorber (with the lowest resonance frequency), $\omega \approx \omega_1 < \omega_n$ $(n = 2,3,\ldots I)$, the damping force of all absorbers except the 1st absorber can be omitted. At the same time, making $\gamma_n = 1$ $(n = 2,3,\ldots I)$, $\mathbb{M}_1$ in Eq. (8) does not contain any unknown parameters.

So far, $\mathbb{M}_1$ is a known function of s. Expanding $\mathbb{M}_1$ by Taylor series at $s = \mathrm{j}\Omega_1$ and keeping only the first term, we can obtain a constant $\mathbb{M}_1(s = \mathrm{j}\Omega_1)$. Then the fixed-point theory represented by Eq. (9) can be used to determine the optimal values of γ_1 and ξ_1 analytically. Having completed the design of the 1st absorber, we can then proceed to the 2nd absorber. Similarly, making $\gamma_n = 1,\ \xi_n = 0$ $(n = 3,4,\ldots I)$ and $s = \mathrm{j}\Omega_2$, and substituting parameters of the 1st absorber obtained in the last step into Eq. (9), the parameters of the 2nd absorber can then be analytically determined. Repeat this procedure one by one until the parameters of all absorbers are obtained, as shown in Eq. (21).

$$\begin{cases} \omega_i = \dfrac{\Omega_i}{1+\sqrt{\left|\dfrac{m_i\vartheta_{i,i}^2}{M_i^{\mathrm{U}}+\sum_{n=1}^{i-1}\dfrac{m_n\vartheta_{i,n}^2\left(2\mathrm{j}\xi_n\Omega_i\omega_n+\omega_n^2\right)}{-\Omega_i^2+2\mathrm{j}\xi_n\Omega_i\omega_n+\omega_n^2}+\sum_{n=i+1}^{N}\dfrac{m_n\vartheta_{i,n}^2\Omega_n^2}{-\Omega_i^2+\Omega_n^2}}\right|}} \\ \xi_i = \sqrt{\dfrac{3\left|\dfrac{m_i\vartheta_{i,i}^2}{M_i^{\mathrm{U}}+\sum_{n=1}^{i-1}\dfrac{m_n\vartheta_{i,n}^2\left(2\mathrm{j}\xi_n\Omega_i\omega_n+\omega_n^2\right)}{-\Omega_i^2+2\mathrm{j}\xi_n\Omega_i\omega_n+\omega_n^2}+\sum_{n=i+1}^{N}\dfrac{m_n\vartheta_{i,n}^2\Omega_n^2}{-\Omega_i^2+\Omega_n^2}}\right|}{8\left(1+\dfrac{m_i\vartheta_{i,i}^2}{\left|M_i^{\mathrm{U}}+\sum_{n=1}^{i-1}\dfrac{m_n\vartheta_{i,n}^2\left(2\mathrm{j}\xi_n\Omega_i\omega_n+\omega_n^2\right)}{-\Omega_i^2+2\mathrm{j}\xi_n\Omega_i\omega_n+\omega_n^2}+\sum_{n=i+1}^{N}\dfrac{m_n\vartheta_{i,n}^2\Omega_n^2}{-\Omega_i^2+\Omega_n^2}\right|}\right)}} \end{cases}. \tag{21}$$

By retaining the functional form of $\mathbb{M}_i$ in the design process, the H_∞ method can be used to numerically design absorber parameters, as below:

$$\underset{\omega_i,\xi_i}{\operatorname{argmin}}\left\|\frac{F_i^{U}(s)\Big/\left(\vartheta_{i,i}^2\sigma_i\right)}{s^2\frac{M_i^{\mathrm{U}}+\sum_{n=1}^{i-1}\frac{m_n\vartheta_{i,n}^2\left(2\xi_ns\omega_n+\omega_n^2\right)}{s^2+2\xi_ns\omega_n+\omega_n^2}+\sum_{n=i+1}^{N}\frac{m_n\vartheta_{i,n}^2\omega_n^2}{s^2+\Omega_n^2}}{\vartheta_{i,i}^2}+\frac{K_i^{\mathrm{U}}}{\vartheta_{i,i}^2}+\frac{s^2m_i\left(2\xi_is\omega_i+\omega_i^2\right)}{s^2+2\xi_is\omega_i+\omega_i^2}}\right\|_\infty. \tag{22}$$

2.4. Summary

The proposed model-free sequential design of absorbers to achieve the desired vibration reduction is summarized as follows:

Step 1: Measure/simulate the structural response of structure $\mathbf{X}(s)$.
Step 2: Conduct Singular Value Decomposition (SVD) on the collected response data as shown in Eq. (3), and select the first few singular vectors as the EDRBs to calculate M_i^{U} using Eq. (13). Then determine K_i^{U} by $K_i^{\mathrm{U}} = \left(\Omega_i^{\mathrm{U}}\right)^2M_i^{\mathrm{U}}$, where Ω_i^{U} can be determined by finding peak frequencies of $V_i(s)$.
Step 3: Use the proposed method to decouple absorber location parameters and material parameters. Then select optimal positions according to Fig. 3.
Step 4: Conduct the optimization as shown in Eq. (18) to get the generalized force $F_i^{\mathrm{U}}(s)$.
Step 5: Substitute $F_i^{\mathrm{U}}(s)$ into Eq. (20) to obtain the mass distribution of absorbers to achieve the desired response control.
Step 6: Sequentially design absorbers one by one, according to Eq. (21) or Eq. (22) to get the uncoupled natural frequencies and damping coefficients of the absorbers.

The detailed flowchart of the model-free sequential design of absorbers for customized vibration control is shown in Fig. 5.

It is important to note that the proposed design formalism is applicable to types of dynamic absorbers. Given that the M-K-C dynamic vibration absorber is a widely recognized and well-understood device, it will be used in the subsequent analyses for verification of the proposed method.

3. Numerical simulations and discussions

Three representative case studies are conducted in this section to validate the effectiveness of the proposed design method. The first case involves a rectangular plate, where a stringent response control requirement is applied. This case also compares the performance of absorbers designed using the approaches in Sections 2 with that of two

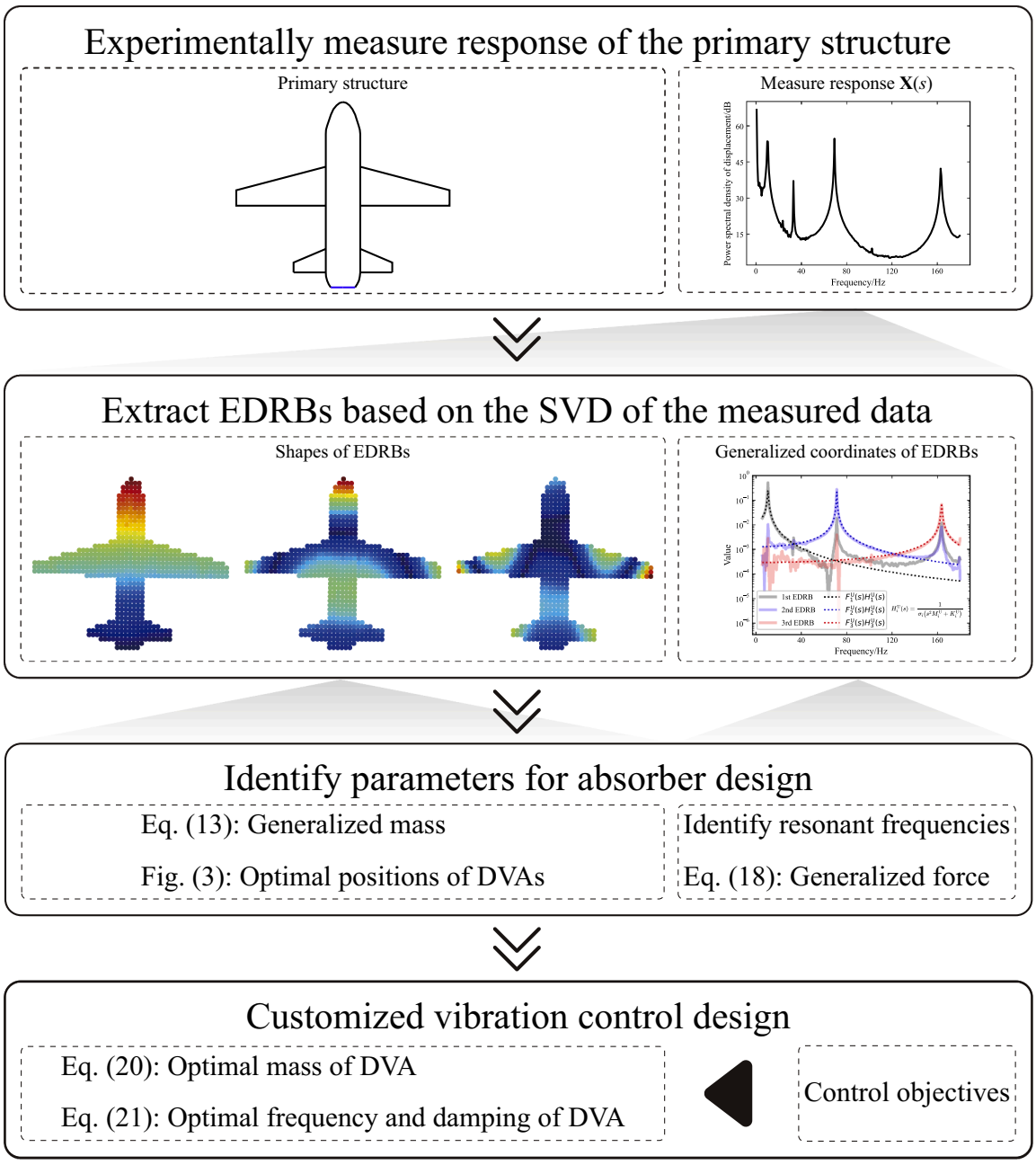

Fig. 5. Flowchart of the model-free sequential design of absorbers for customized vibration control.

existing methods, to demonstrate the superior performance of the proposed design. The second case utilizes a square plate to verify the applicability of the method for structures with symmetric modes and its ability to achieve an all-equal-peak response design. The last case involves a complex rocket fairing structure, illustrating the applicability of the proposed method to more complex structures subjected to distributed loads.

It should be noted that the analytical or finite-element model used in this section serves only to generate response data for absorber design. The mechanical structure itself is not directly utilized in the actual design process.

3.1. Case 1: Customized vibration control of a plate

In this case, a 500 × 200 × 1 mm simply supported rectangular aluminum plate is examined. The plate is excited by a point force at (10 mm,10 mm).

Step 1: The plate vibration response is evaluated at 51 × 21 uniformly distributed points (numerically simulated in this case).

Step 2: Singular Value Decomposition (SVD) is performed on the measured data obtained in **Step 1**, with the first six EDRBs selected for analysis. Shapes and frequencies of these EDRBs are shown in Fig. 6 and Fig. 7, respectively. Calculate M_i^{U} from Eq. (13) using Fig. 6 and obtain Ω_i^{U} by finding the peak frequency of curves in Fig. 7. Then calculate $K_i^{\mathrm{U}} = \left(\Omega_i^{\mathrm{U}}\right)^2 M_i^{\mathrm{U}}$.

Step 3: Select the optimal positions for absorbers according to Fig. 3. Take the 3rd absorber as an example: to obtain its optimal position, the 3rd column of Table 1 is used. According to Fig. 3, the diagonal element $\vartheta_{3,3}$ is first used to filter out positions, which represents the coupling between this absorber and the 3rd EDRB. According to Fig. 6 (c), to make the coupling strong enough, the absorber should be placed in Zone 1, Zone 2 or Zone 3. Since multiple choices are available, we refilter these positions using adjacent elements $\vartheta_{2,3}$ or $\vartheta_{4,3}$. Since the 2nd EDRB has a

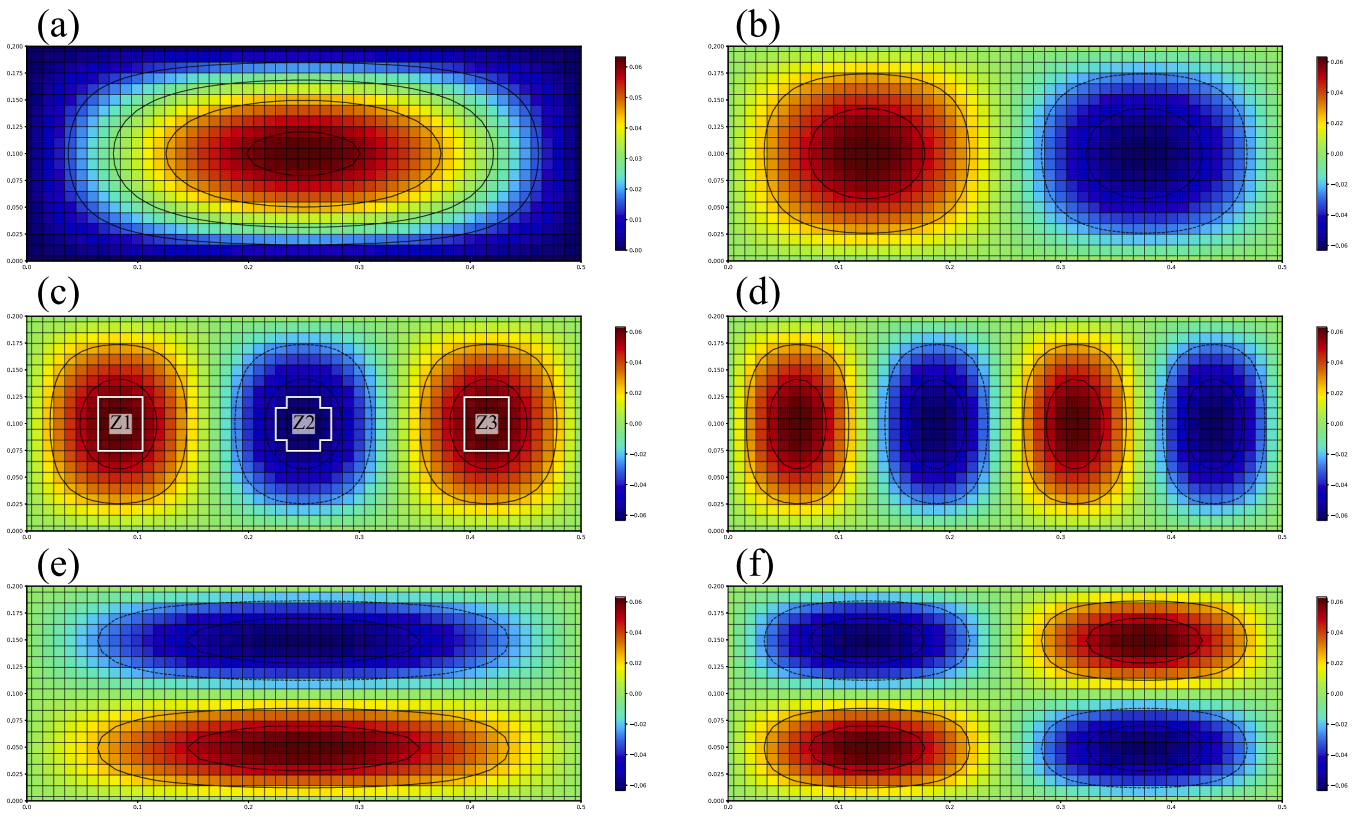

Fig. 6. Shapes of the first six EDRBs, corresponding to the first six columns of **U** in Eq. (3): (a) 1st EDRB, (b) 2nd EDRB, (c) 3rd EDRB, (d) 4th EDRB, (e) 5th EDRB, (f) 6th EDRB.

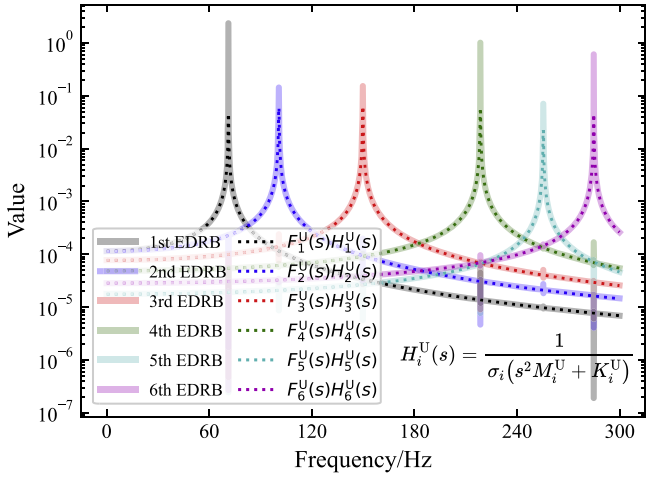

Fig. 7. Generalized coordinates of the six targeted EDRBs as defined by $\mathbf{V}(s)$ in Eq. (3). The y-axis represents the values of the corresponding singular vectors. The close agreement between the curves in the vicinity of resonances demonstrates that the identified force $F_i^U(s)$ effectively characterizes the resonant behavior of the EDRB.

peak frequency much closer to the 3rd EDRB as shown in Fig. 7, the 2nd EDRB will be used to filter positions next. As shown in Table 1, we need to make the coupling between the 2nd EDRB and this absorber $\vartheta_{2,3}$ weak enough, then Zone 1 and Zone 3 should be removed according to Fig. 6. (b). Finally, the central position of Zone 2 is selected as the final optimal location for the 3rd absorber. Similarly, positions for all absorbers can be determined, with results listed in Table 2 and Table 3.

Step 4: Optimize Eq. (18) to obtain $F_i^U(s)$. Substituted into $F_i^U(s)\cdot\frac{1}{\sigma_i(s^2M_i^U+K_i^U)}$ and compare the response with $V_i(s)$ obtained in Eq. (3) to verify the correctness of this optimization. As shown in Fig. 7, curve of $F_i^U(s)\cdot\frac{1}{\sigma_i(s^2M_i^U+K_i^U)}$ matches well with curve $V_i(s)$ around peak frequency, indicating that the obtained $F_i^U(s)$ can well characterize the resonant response of EDRB.

Step 5: Suppose we aim to design the absorbers in such a way that the maximum displacement amplitudes of the 1st, 3rd and 5th peaks are reduced to 24 dB (where dB is defined in Eq. (23)), and those of the 2nd, 4th and 6th peaks are reduced to 7 dB. This volatile response control

Table 2
Absorber parameters obtained by the proposed sequential design method based on fixed-point theory.

	Location/mm	Mass/kg	Frequency/Hz	Damping ratio
DVA1	(250,100)	1.8E-05	70.6	9.94E-03
DVA2	(370,100)	8.7E-04	99.3	6.89E-02
DVA3	(250,100)	7.9E-06	150.1	6.62E-03
DVA4	(310,100)	1.6E-04	218.0	2.95E-02
DVA5	(250,150)	4.1E-07	255.1	1.51E-03
DVA6	(380,150)	5.4E-05	284.6	1.74E-02

Table 3
Absorber parameters obtained by the proposed sequential design method based on H_∞ numerical optimization.

	Location/mm	Mass/kg	Frequency/Hz	Damping ratio
DVA1	(250,100)	1.8E-05	70.6	9.61E-03
DVA2	(370,100)	8.7E-04	99.3	6.91E-02
DVA3	(250,100)	7.9E-06	150.0	6.62E-03
DVA4	(310,100)	1.6E-04	218.0	2.96E-02
DVA5	(250,150)	4.1E-07	255.1	1.46E-03
DVA6	(380,150)	5.4E-05	284.6	1.73E-02

requirement is presented to verify the design method proposed in Section 2.2. The mass values of the absorbers obtained by Eq. (20) are listed in Table 2 and Table 3.

Substituting Eq. (11) into the decibel conversion yields

$$\mathrm{PSD}_{\mathrm{dB}}(s) = 10\log_{10}\frac{S_{xx}(s)}{P_{ref}^2}, \tag{23}$$

where $P_{ref} = 2 \times 10^{-5}\mathrm{m}^2/\mathrm{Hz}$.

Step 6: According to Eq. (21) and Eq. (22), frequency and damping coefficient of absorber can be obtained as shown in Table 2 and Table 3 respectively.

Fig. 8 illustrates the performance of the absorber designed based on Eqs. (21) and (22). For comparative purposes, results from the two methods reported in Refs. [24] and [41] are also plotted. As these two established methods do not provide a method to determine the absorber mass to achieve customized response control, the mass value derived in **Step 5** is applied to ensure a fair comparison.

The results show that the maximum amplitudes of the 1st, 3rd and 5th resonance peaks are indeed reduced to approximately 24 dB, and those of the 2nd, 4th and 6th resonance peaks roughly down to 7 dB. This demonstrates the efficacy of the proposed method and highlights its capability for achieving customized vibration control. Note the performance of the method proposed by LI et al. [41] is very similar to that of ZHU et al. [24]. This is because a simple structure with well-separated modes is used in this case.

Compared with the parameter design method proposed by ZHU et al. [24], the presented sequential design method can achieve better performance. The method based on the fixed-point theory as shown in Eq. (21) is easier to use since analytical expressions have been obtained for the sequential design of absorbers. The method based on H_∞ numerical optimization as shown in Eq. (22) can achieve better performance as fewer assumptions are made. Performance improvement of the proposed sequential design method compared to that of ZHU et al. [24] is summarized in Table 4. Results show that the proposed sequential design method (Eqs. (21) and (22)) can achieve better performance than the established methods reported in Refs. [24] and [41], resulting in improved performance by a maximum of 5.5 dB and 5.9 dB, respectively.

3.2. Case 2: Customized all-equal-peak vibration control of a square plate

In this case, a 500 × 500 × 1 mm simply supported aluminum plate is used to verify the feasibility of the proposed design method for structure with symmetric modes. A point force at (125 mm,125 mm) is applied to

Table 4
Performance improvement of the proposed sequential design methods compared to the one proposed by ZHU et al. [24].

	1st peak	2nd peak	3rd peak	4th peak	5th peak	6th peak
SD_FP	5.5dB	0.0dB	0.6dB	-0.0dB	4.3dB	0.7dB
SD_H_∞	5.9dB	0.0dB	1.5dB	-0.0dB	4.7dB	0.7dB

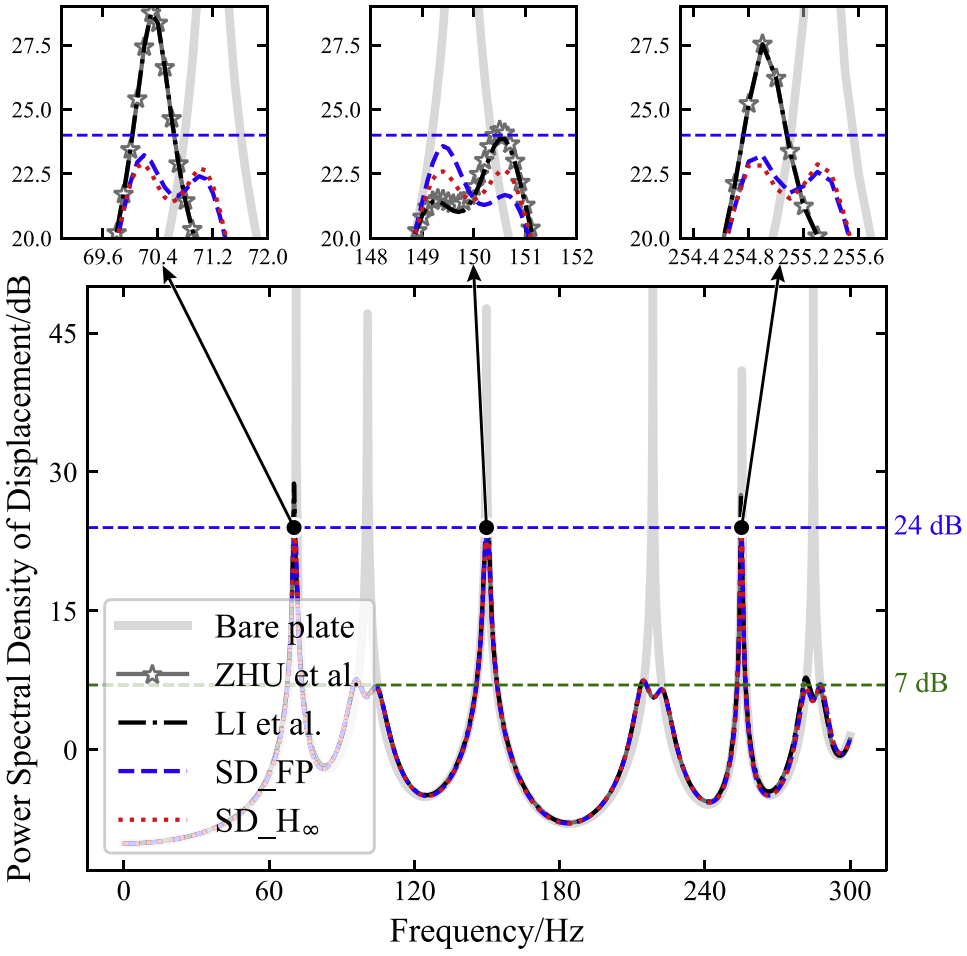

Fig. 8. Power Spectral Density of displacement response of primary structure with different design methods. Response before attaching absorbers is labelled by 'Bare plate', result of method in [24] is labelled by 'ZHU et al.', result of method in [41] is labelled by 'LI et al.', result of Eq. (21) is labelled by 'SD_FP' and result of Eq. (22) is labelled by 'SD_H_∞'. The absorber design aims at controlling the response to 24 dB and 7 dB, respectively.

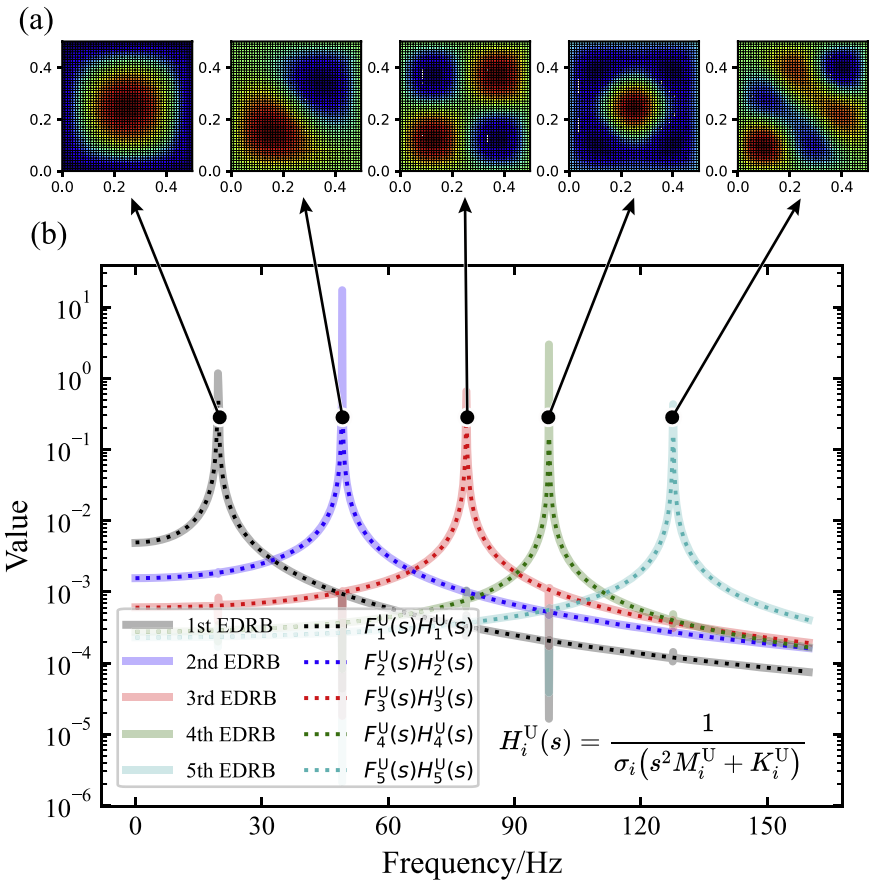

Fig. 9. Vibration shapes (a) and generalized coordinates (b) of the five targeted EDRBs as defined by **U** and **V**(s) in Eq. (3). The y-axis in (b) represents the values of the corresponding singular vectors. The close agreement between the curves in the vicinity of resonances demonstrates that the identified force $F_i^{\mathrm{U}}(s)$ effectively characterizes the resonant behavior of the EDRB.

this structure.

Imposing equal peak control, the design procedure is very similar to Case 1, so only results are shown in this Section. The first 5 EDRBs are shown in Fig. 9, showing that the curve of $F_i^{\mathrm{U}}(s)\cdot\frac{1}{\sigma_i\left(s^2M_i^{\mathrm{U}}+K_i^{\mathrm{U}}\right)}$ matches well with curve $V_i(s)$ around peak frequencies.

Since accurate force identification is crucial for the inverse design of absorbers, the robustness of the proposed identification procedure is investigated under varying spatial measurement resolutions. Moreover, recognizing that measurement noise is inevitable in real-world engineering applications, the method's performance is also evaluated in the presence of noise to assess its practical applicability. The contaminated response is simulated by adding Gaussian white noise to the clean data as follows:

$$\mathbf{X}_{\mathrm{noise}} = \mathbf{X} + \alpha\sigma_{\mathbf{X}}\cdot\varepsilon, \tag{24}$$

where $\mathbf{X}$ is the original structural response; $\mathbf{X}_{\mathrm{noise}}$ the noise-contaminated response; ε a matrix of independent standard normal random variables; $\sigma_{\mathbf{X}}$ the standard deviation of $\mathbf{X}$, and α controls the

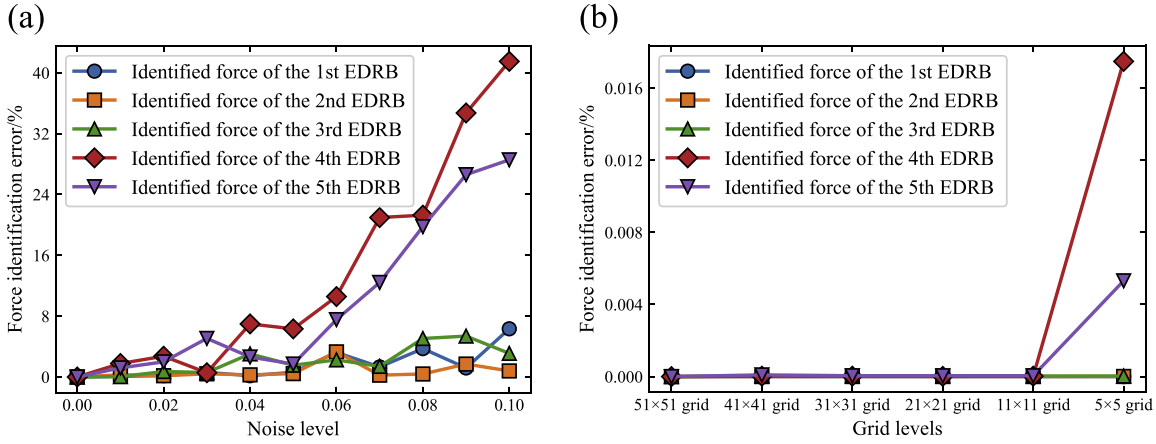

Fig. 10. Force identification error under varying (a) noise levels and (b) measurement grid densities. In the noise sensitivity study (a), the number of measurement points is fixed at 11 × 11.

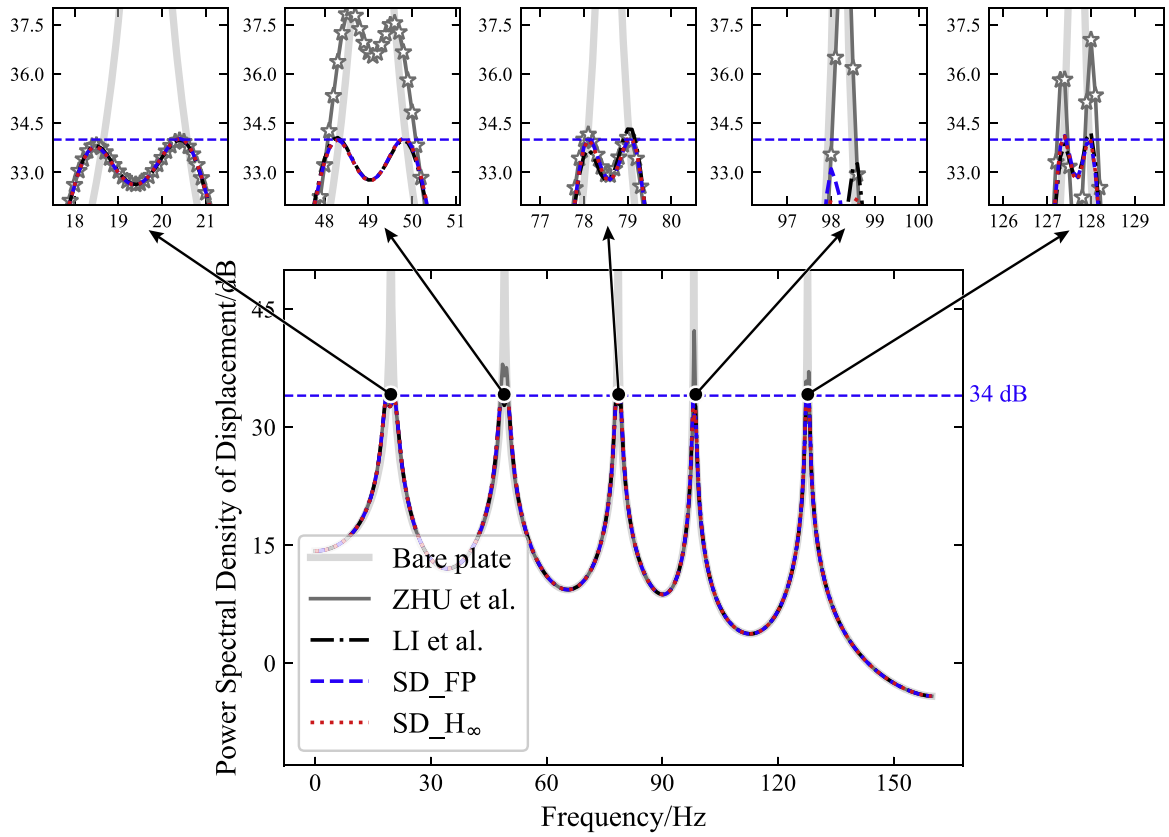

Fig. 11. Power Spectral Density of displacement response of primary structure with different design methods. Response before attaching absorbers is labelled by 'Bare plate', result of method in [24] is labelled by 'ZHU et al.', result of method in [41] is labelled by 'LI et al.', result of Eq. (21) is labelled by 'SD_FP' and result of Eq. (22) is labelled by 'SD_H_∞'. The absorber design aims at controlling all response peaks to 34 dB.

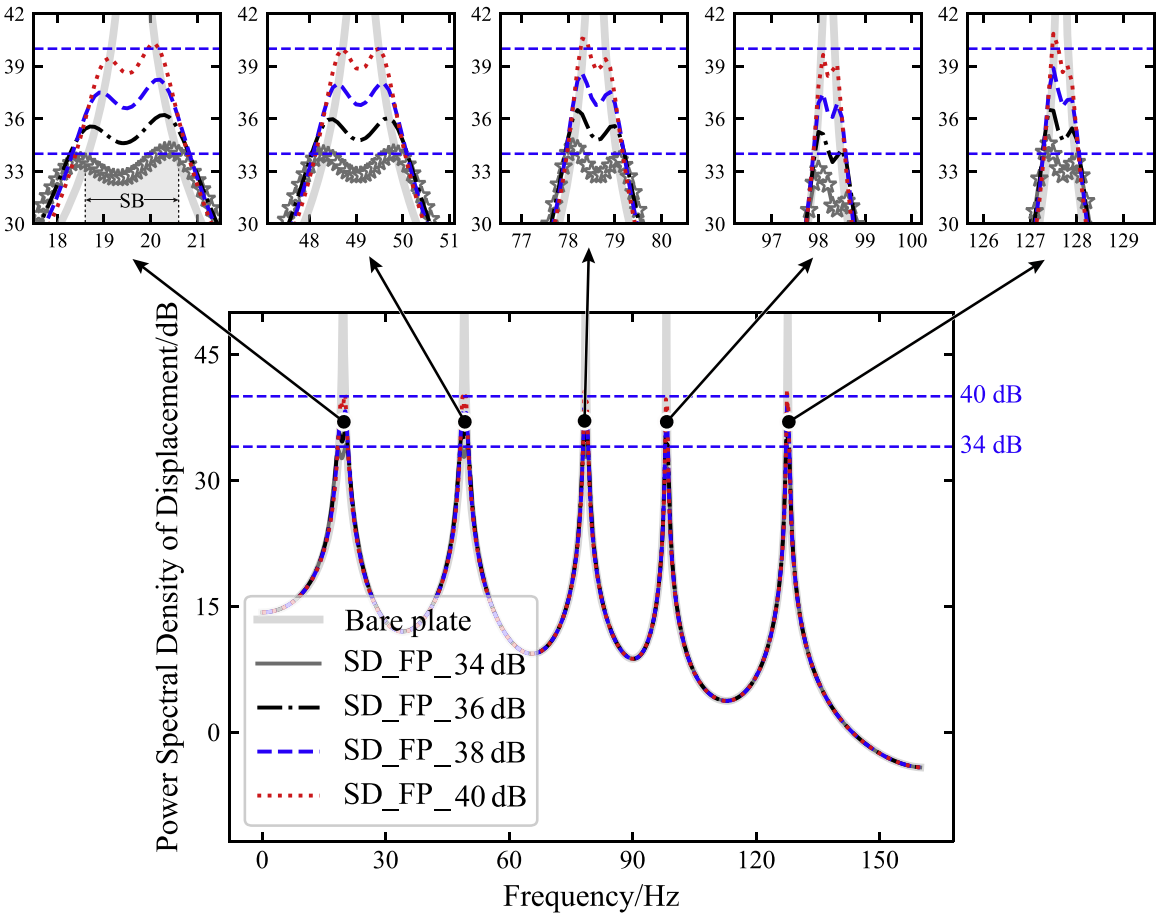

Fig. 12. Power Spectral Density of the displacement response of the primary structure under different design objectives. The response of the uncontrolled structure is labeled "Bare plate," while the responses of the controlled structure, designed to achieve target suppression levels of 34 dB, 36 dB, 38 dB, and 40 dB, are labeled "SD_FP_34 dB," "SD_FP_36 dB," "SD_FP_38 dB," and "SD_FP_40 dB," respectively.

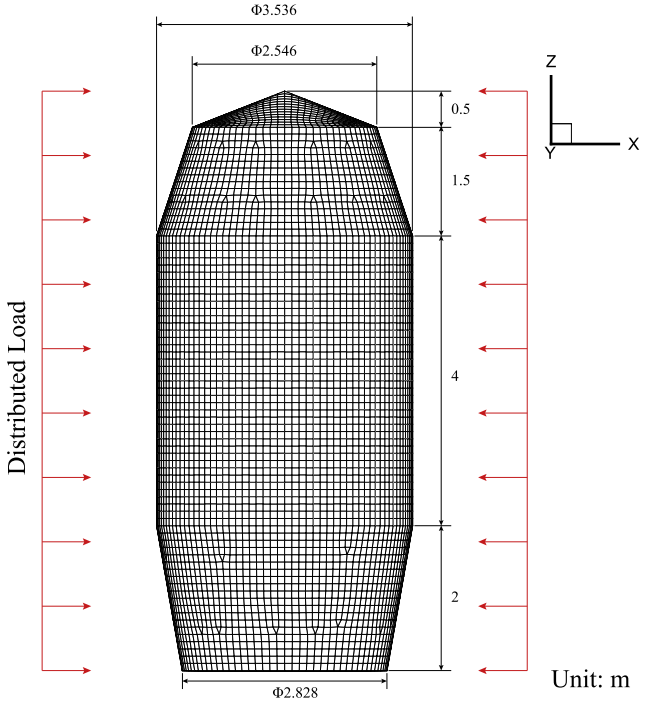

Fig. 13. Dimensions of rocket fairing structure and the distributed load.

noise level.

The force identification error under varying noise levels and measurement grid densities is presented in Fig. 10. The results indicate that when the noise level is below 0.06, the identification error is capped at 15%. At higher noise levels, the forces associated with low-order EDRBs are still identified with reasonable accuracy, whereas those of higher-order EDRBs exhibit significant degradation. This discrepancy arises because the noise assessment is performed using a relatively coarse 11 × 11 measurement grid, which is more susceptible to noise, particularly in the high-frequency range where spatial response variations are finer and more sensitive to spatial distribution. Increasing the number of sensors or optimizing their placement, rather than using a uniform distribution, could mitigate this limitation and improve high-frequency force identification. Since the present study focuses on low-frequency vibration control, a sparser grid (e.g., 5 × 5 points) is sufficient to ensure accurate identification of the dominant EDRBs. In principle, further reduction in the number of measurement points may be achievable through optimal sensor placement. However, such an investigation falls beyond the scope of this paper.

Sequentially designed absorbers yield the final results in Fig. 11. Results of two established methods reported in Refs. [24] and [41] are also included in this figure for comparison. It can be seen that all five resonance peaks have been attenuated till the pre-defined vibration level of 34 dB, which validate that the proposed method can achieve all-equal-peak response design. Besides, the proposed sequential design method can also achieve better performance and can improve the performance by a maximum of 10 dB and 1 dB compared to the methods in [24] and [41].

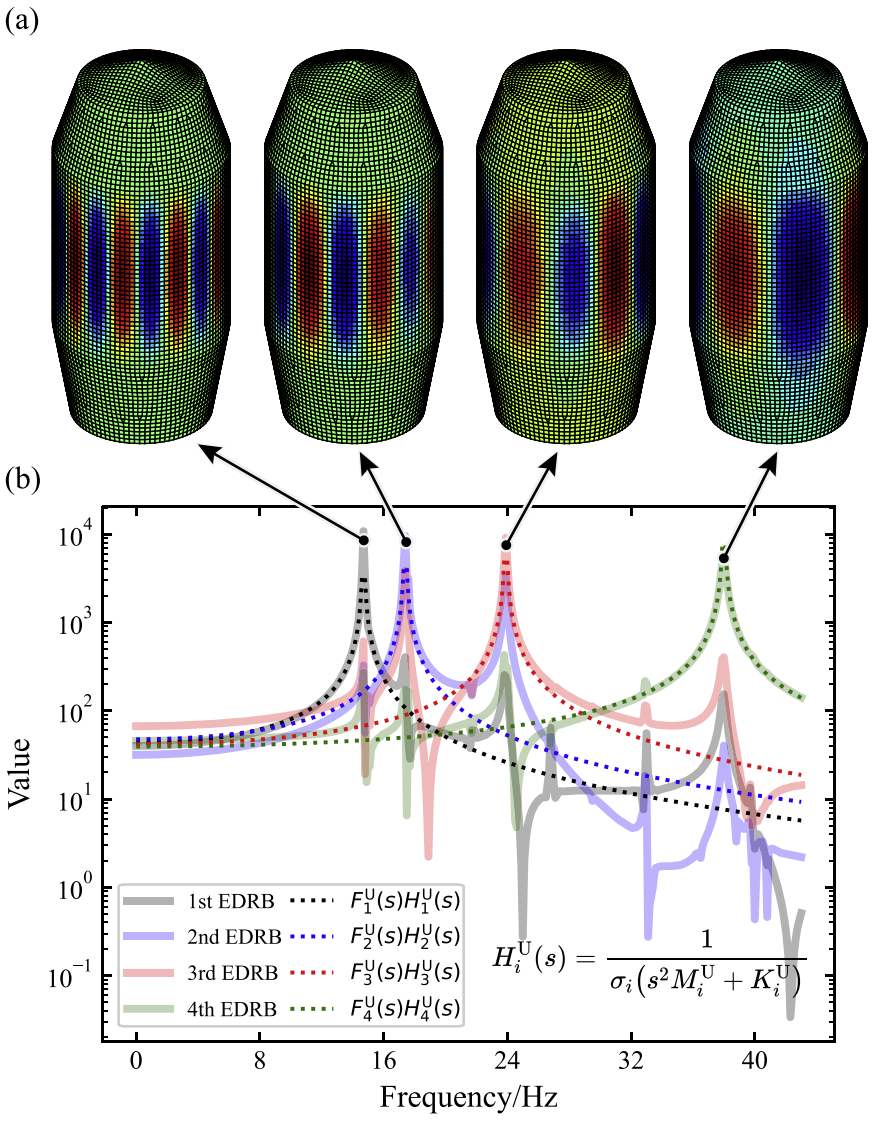

Fig. 14. Vibration shapes (a) and generalized coordinates (b) of the four targeted EDRBs as defined by **U** and **V**(s) in Eq. (3). The y-axis in (b) represents the values of the corresponding singular vectors. The close agreement between the curves in the vicinity of resonances demonstrates that the identified force $F_i^{\mathrm{U}}(s)$ effectively characterizes the resonant behavior of the EDRB.

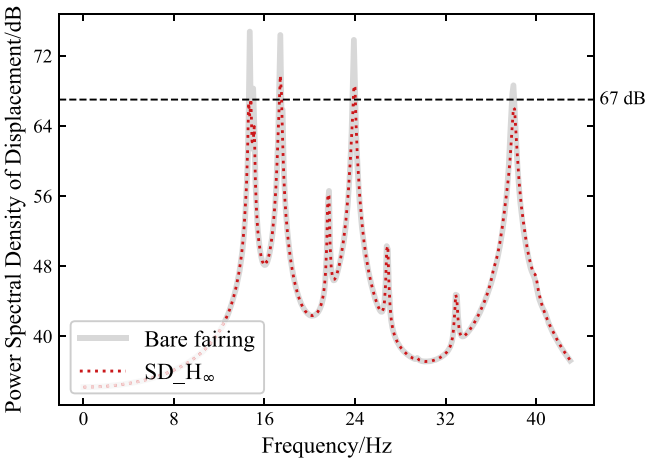

Fig. 15. Power Spectral Density response of primary structure with different design methods. Response before attaching absorbers is labelled by 'Bare fairing' and result obtained by Eq. (22) is labelled by 'SD_H$_\infty$'. The control target is pre-fixed at 67 dB for major resonant peaks.

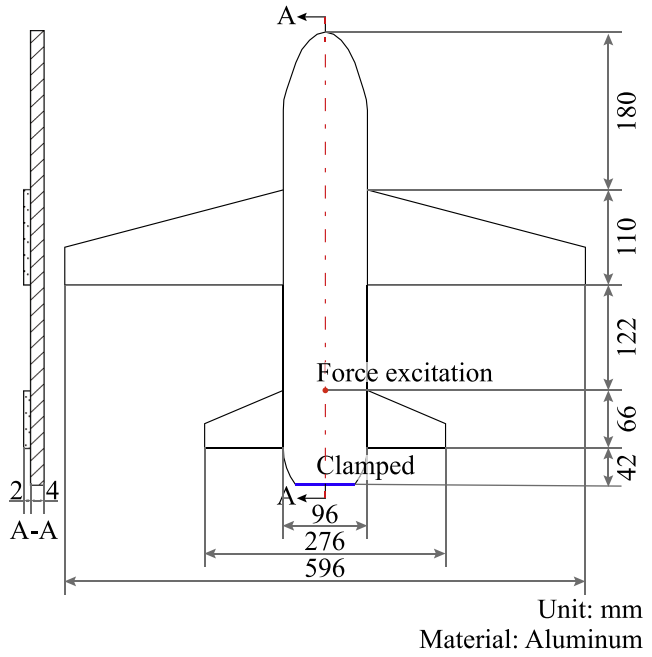

Fig. 16. Scaled-down airplane model.

To verify the robustness of the proposed design method, different vibration control objectives are specified for the inverse design of absorbers. As shown in Fig. 12, the method successfully achieves the desired vibration suppression across all target scenarios. Moreover, the suppression bandwidth, defined as the frequency range over which the controlled response outperforms that of the uncontrolled structure [61], increases with more stringent vibration control requirements.

3.3. Case 3: Customized all-equal-peak vibration control for a rocket fairing structure excited by distributed load

Finally, a rocket fairing structure with distributed load, shown in Fig. 13, is used to verify the applicability of the proposed design method to complex structures with multiple point loads. In the simulation, Rayleigh damping is applied to this structure, thus requiring the use of Eq. (22) through including the damping into the objective function. As a design target, the structural response is limited to a maximum of 67 dB within the frequency range of 0–45 Hz.

The estimated first four EDRBs are shown in Fig. 14. Sequentially designed absorbers according to Eq. (22) yield the final results shown in Fig. 15.

Results show that the structural response within 0-45 Hz has been controlled within 67 dB as targeted. However, response around 17 Hz and 24 Hz slightly exceeds this target, because of two reasons: a) Eq. (20) is derived based on undamped primary system, which is not an exact solution for this structure with damping, although results at 15 Hz and 38 Hz indicate this treatment is still acceptable in most cases; b) As shown in Fig. 14, resonance response at 17 Hz and 24 Hz cannot be perfectly characterized by a single EDRB. The design method shown in Eq. (22) ignores the coupling between different EDRBs, which compromises the optimal result. This problem can possibly be addressed through a more accurate estimation of the EDRB, as well as by revamping Eq. (22) to account for the coupling effects among different EDRBs in the absorber design process.

4. Experimental validations

In this section, experimental validation is performed on a scaled-down airplane model illustrated in Fig. 16. The test sample consists of three panels of uniform thickness (4 mm for the body part and 2 mm for the wing and tail), bolted together over their respective overlapping regions as shown in Fig. 17. The sample is clamped on the tail edge and excited by a point force. Due to the complexity of this model, obtaining an accurate analytical model for absorber design is challenging. This highlights the advantage of the proposed model-free design method. In this experiment, absorbers are designed solely based on the measured structural response data to achieve customized vibration control.

As shown in Fig. 17, the airplane model is excited by an electromechanical shaker, with the applied force measured by a force transducer. The dynamic response of the model, in terms of transverse displacement, is captured by a laser Doppler vibrometer (Polytec PSV-500).

Prior to attaching the absorbers, the dynamic response of the airplane model is measured. According to the design approach established in Section 2, SVD is first applied to identify the generalized force, which is essential for achieving customized vibration control. To verify the accuracy of this identification, the product $F_i^{\mathrm{U}}(s)\cdot\frac{1}{\sigma_i\left(s^2M_i^{\mathrm{U}}+K_i^{\mathrm{U}}\right)}$ is compared with $V_i(s)$, which corresponds to the ith column of $\mathbf{V}(s)$ derived from Eq. (3). As shown in Fig. 18, the identified generalized force accurately captures the resonant behavior of the model.

The design objective is set to limit the maximum displacement amplitude of the first three peaks to 40 dB, 30 dB and 20 dB, respectively. Based on the obtained EDRBs shown in Fig. 18, the absorber masses, tuning frequencies, and damping ratios are determined using Eqs. (20) and (21), yielding the results tabulated in Table 5. The airplane model used in this experiment has a mass of 935.3 g; the three absorbers collectively add 4.36% to this mass. As shown in Fig. 17, the damping of DVA2 and that of DVA3 are implemented by wrapping damping material (Blue-Tack rubber) around the stiffness rod. For DVA1, however, due to its low operating frequency, this damping approach turns out to be ineffective. Instead, a dedicated damping structure (serpentine structure fabricated from Blue-Tack rubber) is attached to the end of its mass block. Because mechanical damping is difficult to apply in a controlled and quantitative manner, the actual damping values of the absorber are not exactly the designed optimal values. This deviation is most pronounced for DVA1, which requires the highest damping ratio, a level that is particularly challenging to achieve at low frequencies.

Before experiment, the absorber masses are measured using an electronic scale. The resonant frequencies and damping ratios of the absorbers are identified from the measured base displacement x_{base} and DVA displacement x_{DVA} shown in Fig. 17 (See Appendix A for more details). The measured and fitted transfer functions of the three absorbers are shown in Fig. 19.

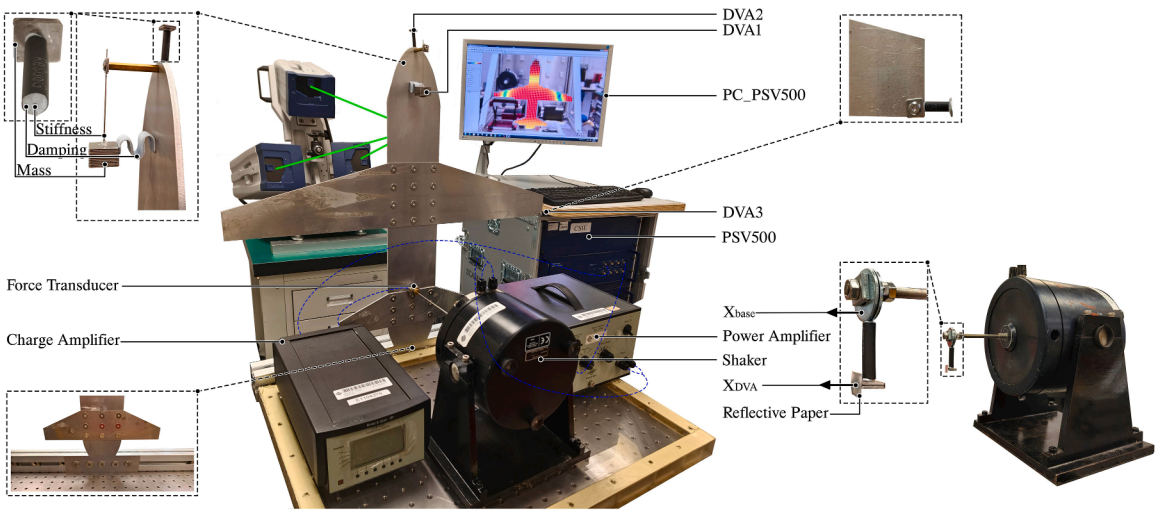

Fig. 17. Experimental setup. The structure is excited by an electromechanical shaker, with its dynamic response measured using a laser Doppler vibrometer. The measurement provides the data to be used in the absorber design.

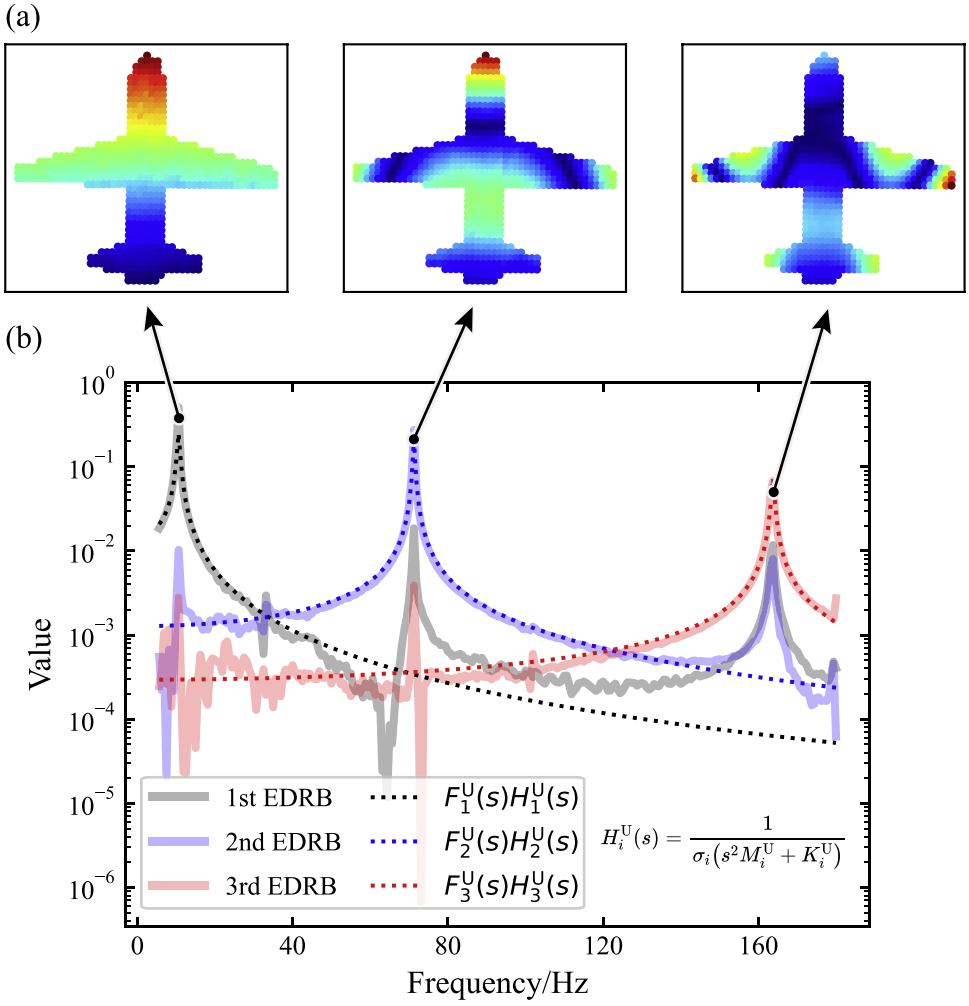

Fig. 18. Vibration shapes (a) and generalized coordinates (b) of the three targeted EDRBs as defined by **U** and **V**(s) in Eq. (3). The y-axis in (b) represents the values of the corresponding singular vectors. The close agreement between the curves in the vicinity of resonances demonstrates that the identified force $F_i^{\mathrm{U}}(s)$ effectively characterizes the resonant behavior of the EDRB.

Table 5
Designed and measured parameters of absorbers.

	Mass/g		Frequency/Hz		Damping ratio	
	Designed	Measured	Designed	Measured	Designed	Measured
DVA1	38.9	38.6	8.84	9.38	0.251	0.103
DVA2	1.5	1.3	70.15	71.88	0.076	0.092
DVA3	0.5	0.5	162.80	162.80	0.047	0.071

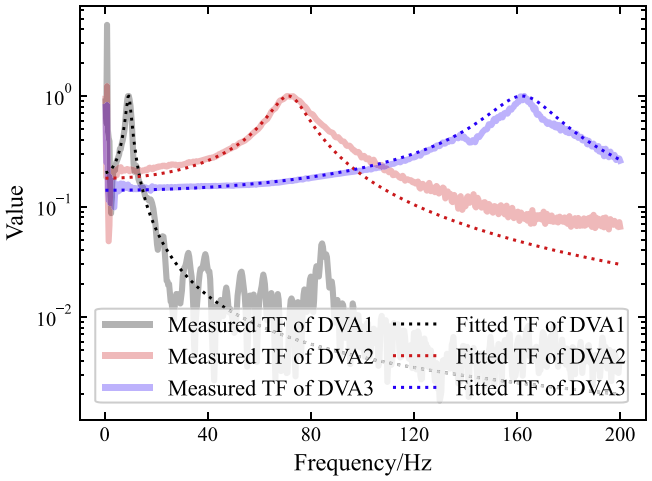

Fig. 19. Measured and fitted transfer functions of absorbers. The close agreement between the curves near resonances demonstrates that the identified absorber frequency and damping accurately represent its dynamic behavior.

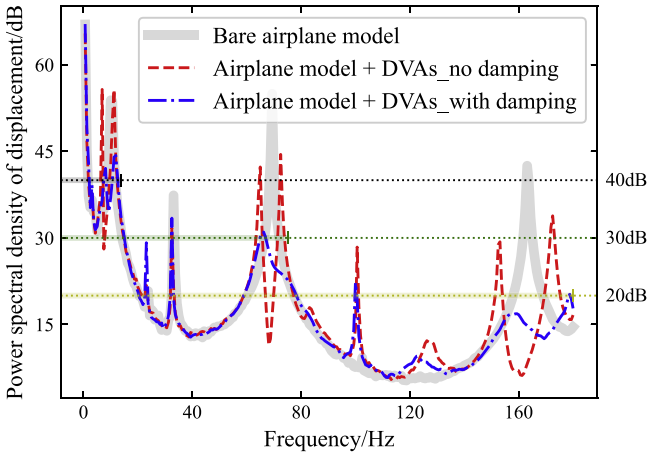

Fig. 20. Power spectral density of the structural displacement. The response before attaching the absorbers is labeled 'Bare airplane model', while the response after attaching the designed absorbers is labeled 'Airplane model + DVAs_with damping'. For comparison, the response with the absorbers installed but without damping, labeled 'Airplane model + DVAs_no damping', is also included. The absorber design aims at controlling three peak response to 40 dB, 30 dB and 20 dB, respectively.

The overall response (represented by the displacement power spectral density, calculated using Eq. (11) for 575 uniformly distributed measurement points) is presented in Fig. 20. The results demonstrate that the three targeted resonant peaks have been effectively attenuated close to the predefined vibration levels, with the largest deviation for the first peak, which remains above its defined target due to the insufficient damping in DVA1. Nevertheless, the experimental results reasonably confirm the ability of the proposed design method to achieve customized vibration reduction targets.

5. Conclusions

In this paper, based on the experimentally measured structural response of the primary structure, we propose a model-free and sequential approach for the design of distributed absorbers over an arbitrary thin-walled structure. As a component of the design procedure, an inverse method is proposed to achieve customized global broadband vibration control. The effectiveness of the proposed methodology is verified through both numerical analyses and experimental validations. Main conclusions are summarized as follows:

1) The proposed inverse design method offers an effective approach for achieving customized broadband vibration control. The optimization process is straightforward, as the solution can be directly obtained by solving a matrix equation.
2) The absorber location is determined to guarantee a) its maximum coupling with the target EDRB to be controlled; b) weak interaction with the EDRB with lower peak frequencies; and c) strong coupling with the EDRB with higher peak frequencies.
3) Absorber parameters can then be determined sequentially based on the fixed-point theory or H_∞ numerical optimization. The former offers an analytical and easy-to-use solution, while the latter provides superior vibration suppression performance involving fewer simplifying assumptions. Given that absorbers are optimized individually and sequentially, the two unknown parameters for each absorber (uncoupled resonance frequency and damping coefficient) can be straightforwardly derived.
4) Strong coupling can occur between different EDRBs, even when their peak frequencies are well separated. This is due to the similarity in their vibrational shapes (spatial matching). To mitigate this issue, specific requirements should be introduced during the Singular Value Decomposition of the measured response.
5) The proposed design method effectively achieves targeted broadband vibration control and is shown to outperform some existing approaches through comparative analyses.

It should be noted that, though illustrated using examples of dynamic vibration absorbers, the proposed absorber design method is applicable to a broad class of absorber design problems, such as piezoelectric shunt absorbers, Helmholtz resonators etc..

CRediT authorship contribution statement

Hangxing LI: Writing – review & editing, Writing – original draft, Visualization, Validation, Software, Resources, Methodology, Formal analysis, Conceptualization. **Waion WONG:** Writing – review & editing, Writing – original draft, Visualization, Supervision, Project administration, Funding acquisition, Conceptualization. **Li CHENG:** Writing – review & editing, Writing – original draft, Visualization, Validation, Supervision, Project administration, Methodology, Investigation, Funding acquisition, Formal analysis, Conceptualization.

Declaration of competing interest

The authors declare that they have no known competing financial interests or personal relationships that could have appeared to influence the work reported in this paper.

Appendix A. Identification of absorber parameters

As shown in Fig. 21, subject to a displacement excitation x_{base}, the equation of motion for the absorber writes:

$$m_{\text{DVA}}\ddot{x}_{\text{DVA}} = k_{\text{DVA}}(x_{\text{base}} - x_{\text{DVA}}) + c_{\text{DVA}}(\dot{x}_{\text{base}} - \dot{x}_{\text{DVA}}), \tag{25}$$

yielding the transfer function:

$$\text{TF} = \frac{X_{\text{DVA}}}{X_{\text{base}}} = \frac{sc_{\text{DVA}} + k_{\text{DVA}}}{s^2 m_{\text{DVA}} + sc_{\text{DVA}} + k_{\text{DVA}}}. \tag{26}$$

Upon measuring TF, the absorber parameters k_{DVA} and c_{DVA} can be identified by fitting the measured data to Eq. (26).

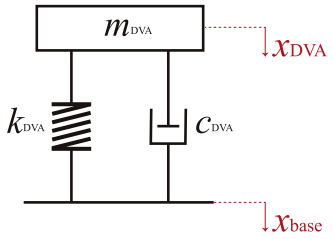

Fig. 21. Model for absorber parameter identification.

Appendix B. Transfer functions of common absorber types

The commonly used vibration absorbers are illustrated in Fig. 22, and their corresponding transfer functions are derived in this section.

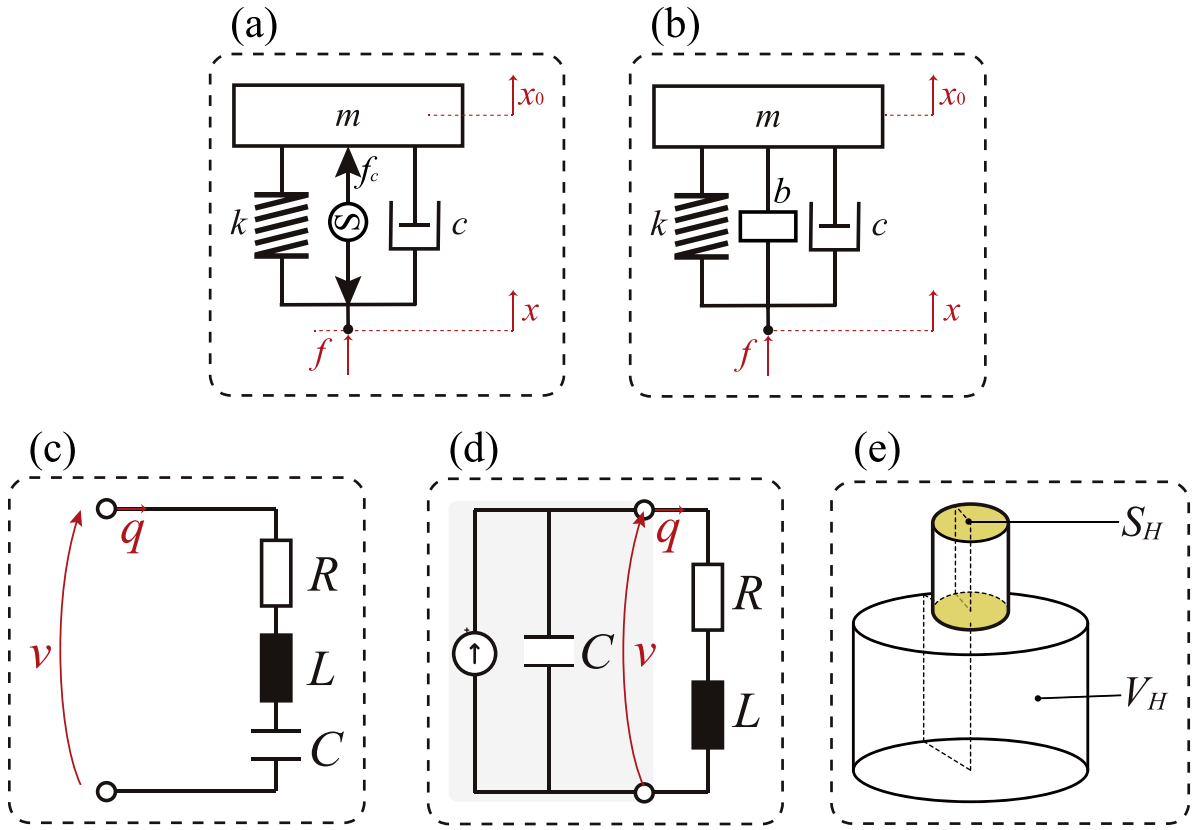

Fig. 22. Common types of vibration absorbers: (a) Active absorber, where m, k, c, and f_c denote the absorber's mass, stiffness, damping, and active control force, respectively; (b) Inerter-based absorber, where m, k, c, and b represent mass, stiffness, damping, and inertance; (c) Electromechanical shunt absorber, with shunt circuit elements R, L, and C denoting the resistor, inductor, and capacitor; (d) Piezoelectric shunt absorber, where C is the inherent capacitance of the piezoelectric patch, and R and L are the shunt resistor and inductor; (e) Helmholtz resonator, where S_H and V_H are the cross-sectional area of the neck and the cavity volume, respectively.

The equation of motion for the active absorber shown in Fig. 22 (a) can be expressed as

$$\begin{aligned} s^2 m x_0 &= (sc+k)(x-x_0)+f_c \\ f &= (sc+k)(x-x_0)+f_c \end{aligned}. \tag{27}$$

Using this equation, the transfer function of the active absorber can be derived as

$$h = \frac{f}{x} = \frac{s^2 m(sc+k)}{s^2 m+sc+k} + \frac{s^2 m}{s^2 m+sc+k} h_c, \tag{28}$$

where $h_c = \frac{f_c}{x}$ denotes the transfer function of the active force actuator.

Similarly, motion equation of the inerter-based absorber shown in Fig. 22 (b) can be expressed as

$$\begin{aligned} s^2 m x_0 &= (sc+sb+k)(x-x_0) \\ f &= (sc+sb+k)(x-x_0) \end{aligned}. \tag{29}$$

The transfer function for this type of absorber can then be derived as

$$h = \frac{f}{x} = \frac{s^2 m(sc+sb+k)}{s^2 m+sc+sb+k}. \tag{30}$$

When an electromagnetic absorber (Fig. 22 (c)) is attached to the primary structure, the generated force can be expressed as $f = sK_{\mathrm{em}}q$, and the voltage across its electrodes as $v = sK_{\mathrm{em}}x$, where K_{em} denotes the motor constant [99–101]. The corresponding transfer function can then be derived as

$$h = \frac{f}{x} = \frac{K_{\mathrm{em}}^2 s^2}{s^2 L+sR+1/C}. \tag{31}$$

For the piezoelectric shunt absorber (Fig. 22 (d)), the transfer function can be expressed in terms of the admittance of the shunt circuit [76] and is derived as

$$h = \frac{s}{sC+Y(s)} = \frac{1}{C}\frac{s^2 L+sR}{s^2 L+sR+1/C}. \tag{32}$$

The Helmholtz resonator (Fig. 22 (e)) can be modelled as an acoustic source with volume velocity q expressed as

$$q = S_H \dot{x}\left(s^2 m+sc+k\right)x = pS_H, \tag{33}$$

where m, k, and c denote the mass, stiffness, and damping of the equivalent lumped-parameter model, and x and p represent the particle displacement and acoustic pressure response near the neck opening, respectively.

Transfer function of Helmholtz resonator can then be expressed as

$$h = \frac{\dot{q}}{p} = \frac{s^2 S_H^2}{s^2 m+sc+k}. \tag{34}$$

Data availability

Data will be made available on request.

References

[1] Escartí-Guillem MS, Garcia-Raffi LM, Hoyas S. Review of launcher lift-off noise prediction and mitigation. Results Eng 2024;23:102679. https://doi.org/10.1016/j.rineng.2024.102679.

[2] Zhu L, Ma J, Wu Y, Liu F, Kang J. Effects of acoustic environment on sleep and mental health in residential regions near railways. Appl Acoust 2025;227:110260. https://doi.org/10.1016/j.apacoust.2024.110260.

[3] Shukla A, Tandel BN, Kajaliya PP. Auditory and mental well-being of teachers in urban noise environment: a partial least square structural equation model approach. Appl Acoust 2025;230:110417. https://doi.org/10.1016/j.apacoust.2024.110417.

[4] Wang X, Luo L, Zhu J, Zou W, Wang T, Fu G, Lu C. Tooth-shape electromagnetic vibration absorber with adjustable positive and negative stiffness. Int J Mech Sci 2025;300:110480. https://doi.org/10.1016/j.ijmecsci.2025.110480.

[5] Su N, Zeng C, Chen Z, Bian J, Xia Y. Multi-modal response control with multiple suspension-type tuned vibration absorbers. Int J Mech Sci 2025;285:109775. https://doi.org/10.1016/j.ijmecsci.2024.109775.

[6] Liu X, Wu JH, Niu J, Li W, Liu C. Vibro-acoustic helmholtz absorber with soft wall for broadband sound absorption. Int J Mech Sci 2025;289:110083. https://doi.org/10.1016/j.ijmecsci.2025.110083.

[7] Tso MH, Yuan J, Wong WO. Design and experimental study of a hybrid vibration absorber for global vibration control. Eng Struct 2013;56:1058–69. https://doi.org/10.1016/j.engstruct.2013.06.017.

[8] Barredo E, Mendoza Larios JG, Mayén J, Flores-Hernández AA, Colín J, Montiel MA. Optimal design for high-performance passive dynamic vibration absorbers under random vibration. Eng Struct 2019;195:469–89. https://doi.org/10.1016/j.engstruct.2019.05.105.

[9] Høgsberg J, Lossouarn B, Deü J-F. Tuning of vibration absorbers by an effective modal coupling factor. Int J Mech Sci 2024;268:109009. https://doi.org/10.1016/j.ijmecsci.2024.109009.

[10] Alsuwaiyan AS, Shaw SW. Performance and dynamic stability of general-path centrifugal pendulum vibration absorbers. J Sound Vib 2002;252:791–815. https://doi.org/10.1006/jsvi.2000.3534.

[11] Cheung YL, Wong WO. $H\infty$ and $H2$ optimizations of a dynamic vibration absorber for suppressing vibrations in plates. J Sound Vib 2009;320:29–42. https://doi.org/10.1016/j.jsv.2008.07.024.

[12] Du Y, Zou T, Pang F, Hu C, Ma Y, Li H. Design method for distributed dynamic vibration absorbers of stiffened plate under different boundary constraints. Thin-Walled Struct 2023;185:110494. https://doi.org/10.1016/j.tws.2022.110494.

[13] Dogan H, Sims ND, Wagg DJ. Design, testing and analysis of a pivoted-bar inerter device used as a vibration absorber. Mech Syst Signal Process 2022;171:108893. https://doi.org/10.1016/j.ymssp.2022.108893.

[14] Dietrich J, Raze G, Kerschen G. Multimodal shunt damping of mechanical structures using multiple digital vibration absorbers. Eng Res Express 2022;4:045028. https://doi.org/10.1088/2631-8695/ac9fa8.

[15] Zhu J, Dai S, Wang K, Mao J, Qu Y, Meng G. A multi-directional sound absorber for suppressing broadband finite-amplitude acoustic waves. Int J Mech Sci 2025;299:110393. https://doi.org/10.1016/j.ijmecsci.2025.110393.

[16] Guo H, Cao Z, Yang T, Chen L-Q. A variable-thickness-arch based nonlinear vibration absorber for rotor-bearing systems. Mech Syst Signal Process 2025;224:111979. https://doi.org/10.1016/j.ymssp.2024.111979.

[17] Xu H, Ren C, He D, Zhou B, Wang Q, Gao H, Wang T. Coupling vibration characteristics and vibration suppression of rolling mill rolls with dynamic vibration absorber. J Manuf Process 2024;120:1157–79. https://doi.org/10.1016/j.jmapro.2024.04.066.

[18] Basta E, Gupta SK, Barry O. Frequency lock-in control and mitigation of nonlinear vortex-induced vibrations of an airfoil structure using a conserved-mass linear vibration absorber. Nonlinear Dyn 2024;112:8789–809. https://doi.org/10.1007/s11071-024-09543-6.

[19] Brötz N, Rexer M, Puff N, Pelz PF. Fluid dynamic vibration absorber for vehicle suspension system. Veh Syst Dyn 2024;62:1122–41. https://doi.org/10.1080/00423114.2023.2223325.

[20] Li C. Optimum multiple tuned mass dampers for structures under the ground acceleration based on DDMF and ADMF. Earthq Eng Struct Dyn 2002;31:897–919. https://doi.org/10.1002/eqe.128.

[21] Cheung YL, Wong WO, Cheng L. A subsystem approach for analysis of dynamic vibration absorbers suppressing broadband vibration. J Sound Vib 2015;342:75–89. https://doi.org/10.1016/j.jsv.2014.12.039.

[22] Pisano M, Turco E, Petrone G, Gardonio P, De Rosa S. Number vs size of electro-mechanical tuneable vibration absorbers for aeronautical applications: a case study. J Sound Vib 2023;561:117827. https://doi.org/10.1016/j.jsv.2023.117827.

[23] Konda Rodrigues G, Gardonio P, Dal Bo L, Turco E. Multimodal vibration control with piezoelectric patches connected to self-tuning RLC shunts. Mech Adv Mater Struct 2023;30:1050–63. https://doi.org/10.1080/15376494.2022.2136806.

[24] Zhu X, Chen Z, Jiao Y. Optimizations of distributed dynamic vibration absorbers for suppressing vibrations in plates. J Low Freq Noise Vib Act Control 2018;37:1188–200. https://doi.org/10.1177/1461348418794563.

[25] Dayou J. Fixed-points theory for global vibration control using vibration neutralizer. J Sound Vib 2006;292:765–76. https://doi.org/10.1016/j.jsv.2005.08.032.

[26] Su N, Chen Z, Xia Y, Bian J. Hybrid analytical *H*-norm optimization approach for dynamic vibration absorbers. Int J Mech Sci 2024;264:108796. https://doi.org/10.1016/j.ijmecsci.2023.108796.

[27] Frahm H. Device for damping vibrations of bodies. Google Patents; 1911.

[28] Ormondroyd J, Den Hartog JP. The theory of the dynamic vibration absorber. Trans Am Soc Mech Eng 1928;49–50:021007. https://doi.org/10.1115/1.4058553.

[29] Gardonio P, Turco E. Tuning of vibration absorbers and Helmholtz resonators based on modal density/overlap parameters of distributed mechanical and acoustic systems. J Sound Vib 2019;451:32–70. https://doi.org/10.1016/j.jsv.2019.03.015.

[30] Mayou A, Denoël V. Asymptotic analysis of multiple mode structures equipped with multiple tuned mass dampers. J Sound Vib 2022;535:117104. https://doi.org/10.1016/j.jsv.2022.117104.

[31] Li C, Zhao J, Pan H, Cao L, Guan Q, Xu Z-D. Deep reinforcement learning based performance optimization of hybrid system for base-isolated structure and shape memory alloy-inerter. Eng Struct 2025;334:120244. https://doi.org/10.1016/j.engstruct.2025.120244.

[32] Cao L, Pan H, Li X, Li C. Predicting optimal primary tuning parameters of PTTMDI for vortex-induced vibration control of super-tall buildings using physics information enhanced DNN. Eng Struct 2025;334:120268. https://doi.org/10.1016/j.engstruct.2025.120268.

[33] Abé M, Igusa T. Tuned mass dampers for structures with closely spaced natural frequencies. Earthq Eng Struct Dyn 1995;24:247–61. https://doi.org/10.1002/eqe.4290240209.

[34] Zuo L, Nayfeh SA. Optimization of the individual stiffness and damping parameters in multiple-tuned-mass-damper systems. J Vib Acoust 2005;127:77–83. https://doi.org/10.1115/1.1855929.

[35] Hoang N, Warnitchai P. Design of multiple tuned mass dampers by using a numerical optimizer. Earthq Eng Struct Dyn 2005;34:125–44. https://doi.org/10.1002/eqe.413.

[36] Dinh V-N, Basu B. Passive control of floating offshore wind turbine nacelle and spar vibrations by multiple tuned mass dampers. Struct Control Health Monit 2015;22:152–76. https://doi.org/10.1002/stc.1666.

[37] Raze G, Kerschen G. H∞ optimization of multiple tuned mass dampers for multimodal vibration control. Comput Struct 2021;248:106485. https://doi.org/10.1016/j.compstruc.2021.106485.

[38] Wu S, Zheng Y, Geng Y. Time-varying statistics identification of nonstationary random fluctuating pressure via orthogonal polynomial representation and Karhunen–Loève expansion. J Aerosp Eng 2023;36:04023081. https://doi.org/10.1061/JAEEEZ.ASENG-4672.

[39] He Z, Wu S. Model updating of a plate structure in thermal environments using LR-SVR combined with particle swarm optimization. Mech Syst Signal Process 2025;224:112152. https://doi.org/10.1016/j.ymssp.2024.112152.

[40] Li H, Wu S, Chen Q, Fei Q. Design of dynamic absorbers to control the flexural resonant vibration of structures characterized by multiple natural modes. J Sound Vib 2021;513:116415. https://doi.org/10.1016/j.jsv.2021.116415.

[41] Wu S, Li H. A data-driven design method of distributed dynamic vibration absorber for broadband vibration suppression of thin-walled structures. Thin-Walled Struct 2023;182:110264. https://doi.org/10.1016/j.tws.2022.110264.

[42] Mantakas A, Kalderon M, Chondrogiannis KA, Kapasakalis KA, Chatzi E, Antoniadis IA, Sapountzakis EJ. Experimental testing and numerical validation of the extended KDamper: a negative stiffness-based vibration absorber. Eng Struct 2024;321:118894. https://doi.org/10.1016/j.engstruct.2024.118894.

[43] Xiao Y, Shen W, Zhu H, Du Y. An acoustic black hole absorber for rail vibration suppression: simulation and full-scale experiment. Eng Struct 2024;304:117647. https://doi.org/10.1016/j.engstruct.2024.117647.

[44] Mao Q, Yuan W, Wu J. Design and experimental study of a multiple-degree-of-freedom vibration absorber by using an inertial actuator. Int J Struct Stab Dyn 2024;24:2450006. https://doi.org/10.1142/S0219455424500068.

[45] Chen X, Leng Y, Fan S, Su X, Sun S, Xu J, Sun F. Research on dynamic characteristics of a novel triple-magnet magnetic suspension dynamic vibration absorber. J Vib Control 2024;30:1511–23. https://doi.org/10.1177/10775463231164440.

[46] Sui P, Shen Y, Yang S, Wang J. Parameters optimization of dynamic vibration absorber based on grounded stiffness, inerter, and amplifying mechanism. J Vib Control 2022;28:3767–79. https://doi.org/10.1177/10775463211038272.

[47] Lu Z, Rong K, Tian L, Qiu C, Du J. Studies on the damping mechanism of shape memory alloy-spring tuned vibration absorber attached to a multi-degree-of-freedom structure. J Vib Control 2022;28:2666–77. https://doi.org/10.1177/10775463211018526.

[48] Rincon C, Alencastre J, Rivera R. Analytical modelling of an active vibration absorber for a beam. Mathematics 2023;11:2009. https://doi.org/10.3390/math11092009.

[49] Wang K, Shi L, Zou H, Zhao S, Shen C, Lu J. A broadband active sound absorber with adjustable absorption coefficient and bandwidth. J Acoust Soc Am 2024;156:1048–57. https://doi.org/10.1121/10.0028196.

[50] Punyakaew S. Active pendulum vibration absorber utilizing a rotating inertia actuator with time delay in the position feedback. Adv Mech Eng 2024;16:16878132241302029. https://doi.org/10.1177/16878132241302029.

[51] Xu J, Zhou W, Jing J. An electromagnetic torsion active vibration absorber based on the FxLMS algorithm. J Sound Vib 2022;524:116734. https://doi.org/10.1016/j.jsv.2021.116734.

[52] Xu K, Li Z, Ren S, Fang G, Bi K, Han Q. Enhancing the flutter performance of long-span bridges through using inerter-based dynamic vibration absorbers. Eng Struct 2025;328:119733. https://doi.org/10.1016/j.engstruct.2025.119733.

[53] Alotta G, Failla G. Improved inerter-based vibration absorbers. Int J Mech Sci 2021;192:106087. https://doi.org/10.1016/j.ijmecsci.2020.106087.

[54] Su N, Bian J, Chen Z, Xia Y. A novel lever-type inerter-based vibration absorber. Int J Mech Sci 2023;254:108440. https://doi.org/10.1016/j.ijmecsci.2023.108440.

[55] Hu Y, Chen MZQ. Performance evaluation for inerter-based dynamic vibration absorbers. Int J Mech Sci 2015;99:297–307. https://doi.org/10.1016/j.ijmecsci.2015.06.003.

[56] Baduidana M, Kenfack-Jiotsa A. Optimum design for a novel inerter-based vibration absorber with an amplified inertance and grounded stiffness for enhanced vibration control. J Vib Control 2022;28:2502–18. https://doi.org/10.1177/10775463211013221.

[57] He H, Hao L, Zhou Y, Lin Z, Xiang Y, Li Y. Equivalent damping ratio oriented investigation on tuned negative stiffness inerter damper for seismic application. J Sound Vib 2024;589:118538. https://doi.org/10.1016/j.jsv.2024.118538.

[58] Su N, Bian J, Peng S, Chen Z, Xia Y. Analytical optimal design of inerter-based vibration absorbers with negative stiffness balancing static amplification and dynamic reduction effects. Mech Syst Signal Process 2023;192:110235. https://doi.org/10.1016/j.ymssp.2023.110235.

[59] Chen L, Nagarajaiah S, Sun L. A unified analysis of negative stiffness dampers and inerter-based absorbers for multimode cable vibration control. J Sound Vib 2021;494:115814. https://doi.org/10.1016/j.jsv.2020.115814.

[60] Cao L, Li C. Tuned tandem mass dampers-inerters with broadband high effectiveness for structures under white noise base excitations, struct. Control Health Monit 2019;26:e2319. https://doi.org/10.1002/stc.2319.

[61] Cao L, Li X, Huang Y, Li C, Pan H. High robust eddy current tuned tandem mass dampers-inerters for structures under the ground acceleration. Soil Dyn Earthq Eng 2025;188:109040. https://doi.org/10.1016/j.soildyn.2024.109040.

[62] Sun R, Wong W, Cheng L. Tunable electromagnetic shunt damper with opposing magnets configuration. Smart Mater Struct 2020;29:115034. https://doi.org/10.1088/1361-665X/abb21d.

[63] Sun R, Wong W, Cheng L. A tunable hybrid damper with Coulomb friction and electromagnetic shunt damping. J Sound Vib 2022;524:116778. https://doi.org/10.1016/j.jsv.2022.116778.

[64] Auleley M, Thomas O, Giraud-Audine C, Mahé H. Enhancement of a dynamic vibration absorber by means of an electromagnetic shunt. J Intell Mater Syst Struct 2021;32:331–54. https://doi.org/10.1177/1045389X20957097.

[65] Cheng T-H, Oh I-K. A current-flowing electromagnetic shunt damper for multi-mode vibration control of cantilever beams. Smart Mater Struct 2009;18:095036. https://doi.org/10.1088/0964-1726/18/9/095036.

[66] Dal Bo L, Turco E, Gardonio P, Konda Rodrigues G. Electromagnetic and piezoelectric time-varying units for the control of flexural vibrations of thin-walled structures. Mech Adv Mater Struct 2023;30:1083–94. https://doi.org/10.1080/15376494.2022.2120224.

[67] Wang X, Wang D, Li F, Zhang Y, Xu Z, Wang T, Fu G, Lu C. Self-learning vibration absorber with negative electromagnetic stiffness for variable vibration. Int J Mech Sci 2023;248:108225. https://doi.org/10.1016/j.ijmecsci.2023.108225.

[68] Mohamed KS, Amri F, Elboraey MM, Nordin NHD, Abdul Muthalif AG. Adaptive electromagnetic vibration absorber for a multimode structure. Stroj Vestn - J Mech Eng 2022;68:9.

[69] Singleton L, Cheer J. An adaptive electrodynamic metamaterial for the absorption of structural vibration. J Sound Vib 2024;582:118414. https://doi.org/10.1016/j.jsv.2024.118414.

[70] Kimura K, Sugiura T. Vibration modal analysis of superconducting levitation with LCR shunt damper. IEEE Trans Appl Supercond 2024;34:1–4. https://doi.org/10.1109/TASC.2024.3356448.

[71] Grzelczyk D, Wojna M, Ogińska E, Wasilewski G, Awrejcewicz J. Numerical and experimental investigation of a magneto-electro-mechanical oscillator with a new magnet – coil interaction model and energy harvesting. J Sound Vib 2024;583:118427. https://doi.org/10.1016/j.jsv.2024.118427.

[72] Huang Y, Li H, Chen K, Deng Z. Multi-objective parameter optimization of electromagnetic shunt damper for high-temperature superconducting maglev vehicle system. J Vib Control 2023:10775463231206869. https://doi.org/10.1177/10775463231206869.

[73] Dal Bo L, Gardonio P, Casagrande DE, Saggini S. Smart panel with sweeping and switching piezoelectric patch vibration absorbers: experimental results. Mech Syst Signal Process 2019;120:308–25. https://doi.org/10.1016/j.ymssp.2018.10.024.
[74] Berardengo M, Høgsberg J, Manzoni S, Vanali M, Brandt A, Godi T. LRLC-shunted piezoelectric vibration absorber. J Sound Vib 2020;474:115268. https://doi.org/10.1016/j.jsv.2020.115268.
[75] Gardonio P, Casagrande D. Shunted piezoelectric patch vibration absorber on two-dimensional thin structures: tuning considerations. J Sound Vib 2017;395:26–47. https://doi.org/10.1016/j.jsv.2017.02.019.
[76] Raze G, Dietrich J, Kerschen G. Passive control of multiple structural resonances with piezoelectric vibration absorbers. J Sound Vib 2021;515:116490. https://doi.org/10.1016/j.jsv.2021.116490.
[77] Anderson DA. Traveling wave controllers on beams and plates using piezoelectric actuators. J Sound Vib 2024;577:118326. https://doi.org/10.1016/j.jsv.2024.118326.
[78] Bricault C, Pézerat C, Collet M, Pyskir A, Perrard P, Matten G, Romero-García V. Multimodal reduction of acoustic radiation of thin plates by using a single piezoelectric patch with a negative capacitance shunt. Appl Acoust 2019;145:320–7. https://doi.org/10.1016/j.apacoust.2018.10.016.
[79] Jia X, Jin G, Ye T, Chen Y. Tunable underwater sound absorption via piezoelectric materials with local resonators. Int J Mech Sci 2025;285:109812. https://doi.org/10.1016/j.ijmecsci.2024.109812.
[80] Li H, Wong W, Cheng L. Customized broadband structural vibration control using piezoelectric shunt absorbers. Smart Mater Struct 2025;34:115014. https://doi.org/10.1088/1361-665X/ae190f.
[81] Jarlebring E, Sastre J, Ibáñez J. Polynomial approximations for the matrix logarithm with computation graphs. Linear Algebra Appl 2025;721:692–714. https://doi.org/10.1016/j.laa.2024.10.024.
[82] Xia D, Pu X, Tong S, Xu J. Piezoelectric metamaterial with digitally controlled nonlinear shunt circuit for broadband wave attenuation. Appl Phys Lett 2024;124:121704. https://doi.org/10.1063/5.0197609.
[83] Wang C, Yao G, Liu M. Passive vibration control of subsonic thin plate via nonlinear capacitance and negative capacitance coupled piezoelectric shunt damping. Thin Walled Struct 2024;198:111656. https://doi.org/10.1016/j.tws.2024.111656.
[84] Paixão J, Foltête E, Sadoulet-Reboul E, Chevallier G, Cogan S. Self-adaptive piezoelectric vibration absorber with semi-passive tunable resonant shunts. J Sound Vib 2024;583:118424. https://doi.org/10.1016/j.jsv.2024.118424.
[85] Gardonio P, Rodrigues GK. Shunted piezoelectric patch adaptive vibration absorber set to maximise electric power absorption: A comparison between parallel and series RL-shunts. J Vib Control 2024:10775463241246873. https://doi.org/10.1177/10775463241246873.
[86] Raze G, Dietrich J, Lossouarn B, Kerschen G. Modal-based synthesis of passive electrical networks for multimodal piezoelectric damping. Mech Syst Signal Process 2022;176:109120. https://doi.org/10.1016/j.ymssp.2022.109120.
[87] Gao N, Qu S, Li J, Wang J, Chen W. Harnessing post-buckling deformation to tune sound absorption in soft helmholtz absorbers. Int J Mech Sci 2021;208:106695. https://doi.org/10.1016/j.ijmecsci.2021.106695.
[88] Abbad A, Atalla N, Ouisse M, Doutres O. Numerical and experimental investigations on the acoustic performances of membraned helmholtz resonators embedded in a porous matrix. J Sound Vib 2019;459:114873. https://doi.org/10.1016/j.jsv.2019.114873.
[89] Hoppen H, Langfeldt F, Gleine W, von Estorff O. Helmholtz resonator with two resonance frequencies by coupling with a mechanical resonator. J Sound Vib 2023;559:117747. https://doi.org/10.1016/j.jsv.2023.117747.
[90] Estève SJ. Adaptive Helmholtz resonators and passive vibration absorbers for cylinder interior noise control. J Sound Vib 2005;288:1105–30. https://doi.org/10.1016/j.jsv.2005.01.017.
[91] Oblak M, Pirnat M, Boltežar M. Modal-interaction approach to the strong structural–acoustic coupling of an elastic helmholtz resonator and an acoustic cavity containing a heavy fluid. J Sound Vib 2022;535:117120. https://doi.org/10.1016/j.jsv.2022.117120.
[92] Nudehi SS, Duncan GS, Farooq U. Modeling and experimental investigation of a helmholtz resonator with a flexible plate. J Vib Acoust 2013;135. https://doi.org/10.1115/1.4023810.
[93] Morell M, Gourdon E, Collet M, Ture Savadkoohi A, De Bono E, Lamarque C-H. Towards digitally programmed nonlinear electroacoustic resonators for low amplitude sound pressure levels: modeling and experiments. J Sound Vib 2024;584:118437. https://doi.org/10.1016/j.jsv.2024.118437.
[94] Zhang Y, Chang D, Sun H, Yu Z, Cheng X. Vibroacoustic characteristics and control strategies of a fully elastic cavity controlled by piezoelectric shunt oscillators. J Sound Vib 2023;558:117733. https://doi.org/10.1016/j.jsv.2023.117733.
[95] Li X, Cao Z, Xu L, Liu B. Sound absorption of the absorber composed of a shunt loudspeaker and porous materials in tandem. Polymers 2023;15:3051. https://doi.org/10.3390/polym15143051.
[96] Huang L, Wu K, Han X, Zhang Y. Mechanism of low frequency spectral scattering by a side-branch electromagnetic device with switching shunt. J Sound Vib 2023;545:117423. https://doi.org/10.1016/j.jsv.2022.117423.
[97] Zhao H, Zhao D, Dong X. Numerical investigation on acoustic damping characteristics of dual Helmholtz resonators in presence of a grazing flow. J Low Freq Noise Vib Act Control 2024;43:1172–90. https://doi.org/10.1177/14613484241238596.
[98] Wen G, Zhang S, Wang H, Wang Z-P, He J, Chen Z, Liu J, Xie YM. Origami-based acoustic metamaterial for tunable and broadband sound attenuation. Int J Mech Sci 2023;239:107872. https://doi.org/10.1016/j.ijmecsci.2022.107872.
[99] Ao WK, Reynolds P. Analysis and numerical evaluation of H∞ and H2 optimal design schemes for an electromagnetic shunt damper. J Vib Acoust 2019;142. https://doi.org/10.1115/1.4045455.
[100] Ikegame T, Takagi K, Inoue T. Exact solutions to H∞ and H2 optimizations of passive resonant shunt circuit for electromagnetic or piezoelectric shunt damper. J Vib Acoust 2019:141. https://doi.org/10.1115/1.4042819.
[101] Zhu S, Shen W, Qian X. Dynamic analogy between an electromagnetic shunt damper and a tuned mass damper. Smart Mater Struct 2013;22:115018. https://doi.org/10.1088/0964-1726/22/11/115018.